bioRxiv preprint doi: https://doi.org/10.1101/2021.06.22.449380; this version posted June 23, 2021. The copyright holder for this preprint (which was not certified by peer review) is the author/funder, who has granted bioRxiv a license to display the preprint in perpetuity. It is made available under aCC-BY-NC-ND 4.0 International license.

A multiscale approach for computing gated ligand binding from molecular dynamics and Brownian dynamics simulations

S. Kashif Sadiq[1,2,3,*], Abraham Muñiz Chicharro[1,4], Patrick Friedrich[1], Rebecca C. Wade[1,4,5,6],

1 Molecular and Cellular Modeling Group, Heidelberg Institute for Theoretical Studies (HITS), Schloss-Wolfsbrunnenweg 35, 69118 Heidelberg, Germany
2 Genome Biology Unit, European Molecular Biology Laboratory, Meyerhofstrasse 1, 69117 Heidelberg, Germany
3 Infection Biology Unit, Universitat Pompeu Fabra, Barcelona Biomedical Research Park (PRBB), C/Doctor Aiguader 88, 08003 Barcelona, Spain
4 Faculty of Biosciences, Heidelberg University, Im Neuenheimer Feld 234, 69120 Heidelberg, Germany
5 Center for Molecular Biology (ZMBH), DKFZ-ZMBH Alliance, Heidelberg University, Im Neuenheimer Feld 282, 69120 Heidelberg, Germany
6 Interdisciplinary Center for Scientific Computing (IWR), Heidelberg University, Im Neuenheimer Feld 205, 69120 Heidelberg, Germany

* kashif.sadiq@embl.de

Abstract

We develop an approach to characterise the effects of gating by a multi-conformation protein consisting of macrostate conformations that are either accessible or inaccessible to ligand binding. We first construct a Markov state model of the apo-protein from atomistic molecular dynamics simulations from which we identify macrostates and their conformations, compute their relative macrostate populations and interchange kinetics, and structurally characterise them in terms of ligand accessibility. We insert the calculated first-order rate constants for conformational transitions into a multi-state gating theory from which we derive a gating factor γ that quantifies the degree of conformational gating. Applied to HIV-1 protease, our approach yields a kinetic network of three accessible (semi-open, open and wide-open) and two inaccessible (closed and a newly identified, 'parted') macrostate conformations. The 'parted' conformation sterically partitions the active site, suggesting a possible role in product release. We find that the binding kinetics of drugs and drug-like inhibitors to HIV-1 protease falls in the slow gating regime. However, because γ=0.75, conformational gating only modestly slows ligand binding. Brownian dynamics simulations of the diffusional association of eight inhibitors to the protease - that have a wide range of experimental association constants ($\sim 10^4$ - 10^{10} $M^{-1}s^{-1}$) - yields gated rate constants in the range $\sim$0.5-5.7 $\times$ 10^8 $M^{-1}s^{-1}$. This indicates that, whereas the association rate of some inhibitors is described by the model, for most inhibitors the subsequent induced fit step leads to slower association rates. For systems known to be modulated by conformational gating, the approach could be scaled computationally efficiently to screen association kinetics for a large number of ligands.

bioRxiv preprint doi: https://doi.org/10.1101/2021.06.22.449380; this version posted June 23, 2021. The copyright holder for this preprint (which was not certified by peer review) is the author/funder, who has granted bioRxiv a license to display the preprint in perpetuity. It is made available under aCC-BY-NC-ND 4.0 International license.

Introduction

Molecular association is central to virtually all biomolecular processes from regulation of metabolic networks and signal transduction to macromolecular assembly and drug efficacy in pharmacology. Extensive effort over several decades has led to the development of many computational methods to characterize molecular binding affinities [1]. Increasingly, though, the role of binding kinetics, not just affinity, is becoming more widely appreciated in determining the behaviour of biomolecular interaction networks and especially *in vivo* drug efficacy [2, 3].

The binding of two molecules - such as a ligand to a protein - first requires them to encounter each other through a diffusional process, imposing an upper, diffusion-controlled limit - on the association rate [4–6]. Factors such as steric specificity, hydrodynamic interactions and binding site accessibility can all cause reductions from this limit, whilst ligand-protein interaction energies can either enhance or further impede the association rate - for example, through electrostatic steering [5, 7–12]. Dynamic conformational changes in the protein can also alter binding site accessibility by introducing a gating step in the ligand binding process [13–15]. Conformational selection, where the ligand selects a binding site accessible receptor conformation (binding when the gate is open) and induced fit, where the ligand binds a non-accessible conformation and then changes it to an accessible one (opening the gate), may both play a role in the binding process [16–18] and in turn limit the association kinetics.

Gating theory for the interchange between two conformations, open and closed [15, 19–22], suggests the timescale of interchange (τ_c) can play a significant role in conformational selection that depends on whether it is faster ($\tau_c << \tau_d$) or slower ($\tau_c >> \tau_d$) than the characteristic timescale of protein-ligand diffusional encounter (τ_d), or in between. For fast gating, the ligand effectively always encounters the protein in an accessible (open) state - thus the gated (k^g) and ungated (k^{ug}) association rate constants are equal. For slow gating, $k^g = \gamma k^{ug}$, where γ, the gating factor, represents the probability of finding the protein in a ligand-accessible state.

Brownian dynamics (BD) simulation methods offer a computationally inexpensive route for calculating ungated diffusional association kinetics [23], in part due to frequent use of rigid bodies, simplified forcefields and implicit solvent models. They are well-established for protein-protein association rate constants [24, 25] and applied to protein-ligand systems [26, 27]. However, use of rigid structures poses challenges, especially becuase many biomolecular systems exhibit considerable flexibility and where conformational selection and/or induced fit can be a significant contributor to the binding kinetics. Rigid-body BD alone may therefore be applicable to mainly diffusional-limited binders. Multiscale methods that combine BD with molecular dynamics (MD) simulation methods may offer a possible solution to such limitations [26]. A method, known as SEEKR, has been proposed where BD simulations are performed to reach the first milestone, followed by spawning of MD simulations at subsequent milestones [28–31]. Such methods have yet to be tested on proteins with large conformational flexibility.

Furthermore, a plethora of methods have emerged that aim to compute ligand-receptor binding kinetics [32, 33]. Approaches based on molecular dynamics (MD) simulations have become a focal point in this development process [34]. Unbiased high-throughput all-atom MD simulations coupled to Markov state models (MSMs) have proven a rigorous route to extract the kinetics and thermodynamics of biomolecular processes, as well as a detailed description of their respective pathways, including phenomena such as receptor-ligand [17, 35–38], and receptor-receptor binding [39], protein-folding [40–43], conformational changes [37, 44–47] and macromolecular assembly [48].

MSMs usually involve the projection of the high-dimensional conformational space of atomistic features into a lower-dimensional manifold of collective variables (CVs), followed by discretization of the resulting space into non-overlapping microstates. As-

bioRxiv preprint doi: https://doi.org/10.1101/2021.06.22.449380; this version posted June 23, 2021. The copyright holder for this preprint (which was not certified by peer review) is the author/funder, who has granted bioRxiv a license to display the preprint in perpetuity. It is made available under aCC-BY-NC-ND 4.0 International license.

signment of the underlying MD simulation ensemble in terms of a sequence of these microstates allows inter-state transition probabilities to be calculated at time intervals chosen to ensure a memoryless jump process, the condition of 'Markovianity' [49]. The resulting transition matrix, together with methods for further coarse-graining the MSM can then be used to probabilistically group together microstates into a smaller set of macrostates, that represent kinetically distinct interpretable conformations of the system as well as the corresponding coarse-grained equilibrium distribution and transition kinetics [50].

Advantageously, MSMs can account for detailed changes across complex degrees of freedom, such as ligand-receptor binding pathways and therefore quantify the degree of conformational gating and/or induced fit involved [39]. Disadvantageously, they impose a huge computational demand in order to resolve such kinetics accurately. Estimation of association rate constants may require simulating up to $\sim 10^3$-fold longer than the timescale of the binding process [3] due to the dilute solute concentration in a typical MD simulation box. Furthermore, the choice of initial features, the process of dimensionality reduction to obtain CVs and clustering methods for discretisation can all affect the quality of the model [51]. Significant developments have been made in each of these aspects over the last decade [52], including the derivation of a variational principle [53] that enables selection of CVs to be systematized based on maximizing the decorrelation time of linear combinations of atomistic metrics, an approach known as time-independent component analysis, tICA [54–56]. Furthermore, adaptive sampling techniques [57–59] that explore the conformational space more efficiently and neural network approaches that learn optimal CVs [60] can result in orders-of-magnitude reductions in required sampling.

Despite these major developments, application of MSMs remains prohibitive when scaled to multiple numbers of receptor-ligand systems, especially when typical associaton rate constants (k_{on}^{exp}) for many clinically relevant compounds are $k_{on}^{exp} \sim 10^6$ $M^{-1}s^{-1}$ or slower [3]. The high computational demand of unbiased MD has motivated a number of enhanced sampling methods that introduce biasing potentials and/or biased exploration, allowing faster exploration of rarely accessible regions of the conformational space. Recent developments in methods such as metadynamics [61, 62], bias-exchanged metadynamics [63], Gaussian-accelerated molecular dynamics (GAMD) [64], weighted ensemble sampling [65], scaled MD [66] and adaptive multilevel splitting [67] have been applied to rate constant calculations. Unfortunately, such methods either require predefined CVs - which are not always known - or the use of biasing potentials makes recovering the original kinetics challenging [68].

For the class of proteins that exhibit multiple conformational states that may gate ligand binding, we seek here to combine the advantages of MSMs for rigorously computing conformational kinetics with the advantages of BD approaches for rapidly computing ungated rate constants. HIV-1 protease is a suitably flexible, multi-conformation protein on which to develop such an approach and where the relative population, kinetic interchange and functional relevance of different conformations still remain incompletely understood as does the role of such conformations in gating ligand binding. The protease consists of a C_2-symmetric homodimer with a pair of flexible β-hairpin structures, termed 'flaps' that gate access to an active site [69] that structurally recognises [70, 71] and cleaves a number of sequence specific peptidic junctions in viral Gag and GagPol polyproteins [72–74]. Most crystal structures of HIV-1 protease are of ligand-bound complexes - such structures are invariably characterised by a 'closed' flap conformation [75, 76] where the flaps extend beyond but curl towards each other (Figure 1). A handful of apo-protein conformations exist. These include the well-characterised semi-open conformation [77] differentiated by a reversal of flap handedness with respect to the symmetry axis of the dimer - with flaps extending beyond but curling away from

bioRxiv preprint doi: https://doi.org/10.1101/2021.06.22.449380; this version posted June 23, 2021. The copyright holder for this preprint (which was not certified by peer review) is the author/funder, who has granted bioRxiv a license to display the preprint in perpetuity. It is made available under aCC-BY-NC-ND 4.0 International license.

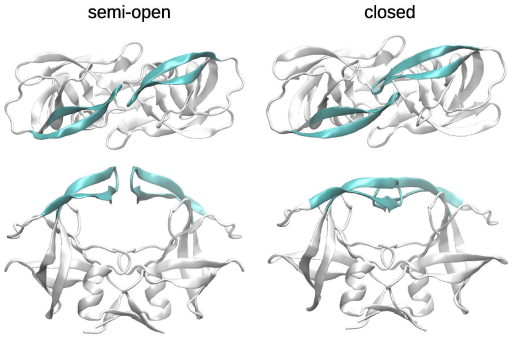

Fig 1. Characteristic conformations of the HIV-1 protease, illustrating a semi-open apo-state (PDB:1HHP) [77] and a closed state (PDB: 1KJ7) [71], required for both substrate cleavage and observed for inhibitor binding. For clarity, the substrate is omitted from the closed state structure depicted here. The homodimeric protein is shown in ribbon representation with the gating flaps in cyan.

each other (Figure 1). A spectrum of more open flap structures [78] exist, marked by an absence of interflap interactions as well as the characteristic closed conformation. Structurally asymmetric conformations and flap dynamics have also been reported [79].

Natural substrate recognition, transition state stabilisation and peptide cleavage occur in the closed conformation [70]. Solution NMR experiments on the apo protein have reported both a fast (<10 ns) and slow ($\sim$100μs) flap transition suggested to be flap tip curling and wide opening, respectively, as well as a dynamic equilibrium between three states of which the semi-open state is the dominant population [80, 81]. More recent NMR studies are inconsistent with this view, reporting a mixture of states where the closed conformation is favoured [82]. Although lateral binding or unbinding of inhibitors, small peptide substrates or auto-associating peptides to either the closed or semi-open conformations may be possible [44, 63, 83, 84], steric considerations require an open state to admit peptidic cleavage sites within Gag or GagPol polyproteins or natural subtrate analogs. MD simulations have also reversibly captured a mixture of closed, semi-open, open and wide-open states in the apo protein - open, characterised by the flaps curling back from semi-open to expose the active site and wide-open, by a significantly larger flap-tip separation [15, 85–87] - with a range of estimated timescales for flap opening ($\sim$10 ns), wide-opening ($\sim$500 ns) and closing ($\sim$50 ns) from a semi-open state.

BD simulations in a coarse-grained model of a two state open-closed system suggested a slow gating regime and showed good agreement with experimental rate constants for a number of inhibitors in the 10^5-10^6 $M^{-1}s^{-1}$ range [15]. However, surface plasmon resonance (SPR) measurements association rate constants for a large array of inhibitors of HIV-1 protease, including the 9 FDA-approved drugs in clinical use [88], showed k_{on}^{exp} values ranging widely from 10^2-10^{10} $M^{-1}s^{-1}$. This suggests that a significant degree of conformational selection, induced fit or both may be at work during ligand binding and possibly in a ligand-dependent way. Furthermore, as more than two states exist and the open state is an intermediate state, then gated binding to an open state would still only be the first step of the process. A second step, requiring some degree of induced-fit-type structural rearrangement is subsequently necessary to arrive at the final bound closed state 2. Simulations have suggested this second induced-fit step may be rate limiting [89] and support the idea that different ligands may vary in their preferred pathway of conformational selection versus induced fit along the first step [90, 91].

Here, using HIV-1 protease as a model system, we report a novel method that combines BD and MSMs built from all-atom MD simulations to calculate the extent of con-

bioRxiv preprint doi: https://doi.org/10.1101/2021.06.22.449380; this version posted June 23, 2021. The copyright holder for this preprint (which was not certified by peer review) is the author/funder, who has granted bioRxiv a license to display the preprint in perpetuity. It is made available under aCC-BY-NC-ND 4.0 International license.

formation gated ligand binding. This is done by combining the two approaches within a theoretical multi-state gating framework for conformational selection. We build on previous gating theory [13–15] to determine a gating factor in terms of the accessible and inaccessible ensemble of conformational macrostates of a MSM. Next we reconstruct the full apo-protein conformational kinetics of HIV-1 PR from a MSM based on all-atom MD simulations, identify accessible and inaccessible states - including a previously unidentified state - from which we obtain the resulting gating factor. Finally, we compute the ungated association kinetics for several ligands binding to each of the set of determined accessible states using BD simulations, applying the theoretical framework to arrive at final gated rate constants. This results in fast and scalable calculations of absolute values of protein-ligand biomolecular association rate constants that approach experimental values, where conformational selection is the dominant factor in limiting binding and allows us to dissect the additional contribution of induced-fit when it is not.

Theory

We build on the theoretical formalism of MSMs [92] and gating theory [13–15], in order to derive a term for the required gating factor to modulate ligand binding association kinetics in terms of the transition kinetics between conformational macrostates exhibited by the unbound target receptor.

Let us consider a Markov state model (MSM) of a stochastic process $\{X_n\}$ which is sufficiently described by a transition matrix $\mathbf{T}$. The elements of the matrix are the conditional probabilities

$$\mathrm{P}_{ij}(\tau) = \mathrm{P}(X_{t_0+\tau} = j | X_{t_0} = i), \tag{1}$$

describing the probability of a transition from a current state i to the next state j within the lag time τ. A MSM fulfilling the Chapman-Kolomogrov equation $\mathbf{T}(n \cdot \tau) = \mathbf{T}(\tau)^n$, in other words a vector holding the description of the state distribution at any time $t = t_0 + n\tau$, can be calculated from an initial distribution $\mathbf{p}(t_0)$ by

$$\mathbf{p}(t)^{\mathrm{T}} = \mathbf{p}(t_0)^{\mathrm{T}} \mathbf{T}(\tau)^n. \tag{2}$$

After sufficient time the probability distribution approaches the stationary distribution $\pi = \mathbf{p}(t \to \infty)$, which contains the probabilities of the single states in equilibrium. Further application of the transition matrix on π has no effect

$$\pi^{\mathrm{T}} = \pi^{\mathrm{T}} \mathbf{T}(\tau), \tag{3}$$

which forms an eigenvector equation. When such a stationary distribution exists a property, the detailed balance, can be derived from Eq.3 and 1.

$$\pi_i \cdot \mathrm{P}_{ij} = \pi_j \cdot \mathrm{P}_{ji}. \tag{4}$$

This property is physically important and describes the reversibility of the MSM.

The MSM transition matrix is estimated from the observed/counted transitions between the states in the single MD simulations. An important parameter for the accuracy of the estimation is the lag time τ. Ideally, the eigenvalues λ_i of the MSM should be independent of τ. Therefore τ should be chosen such that the implied relaxation time scales are approximately constant

$$t_i(\tau) = -\frac{\tau}{\ln|\lambda_i(\tau)|}. \tag{5}$$

bioRxiv preprint doi: https://doi.org/10.1101/2021.06.22.449380; this version posted June 23, 2021. The copyright holder for this preprint (which was not certified by peer review) is the author/funder, who has granted bioRxiv a license to display the preprint in perpetuity. It is made available under aCC-BY-NC-ND 4.0 International license.

To obtain those t_i for a MSM, the lag time might easily exceed the given time scales and therefore our interest lies only in the largest u eigenvalues $\lambda_i(\tau)$, which represent the slowest state transitions. For projected MSMs built on the reduced set of slow-transition eigenvalues, Eq.2 does not in general hold anymore. Rather, in order to coarse-grain an MSM into a meaningful and smaller set of macrostates, a hidden markov model (HMM) can be built to describe u such states at any time step $k\tau$.

The HMM can then be expressed as:

$$\mathbf{P}(k\tau) = \mathbf{\Pi}^{-1}\chi^{\mathrm{T}}\tilde{\mathbf{\Pi}}\tilde{\mathbf{P}}^{k}(\tau)\chi, \tag{6}$$

where $\tilde{\mathbf{P}} \in \mathbb{R}^{u\times u}$ is a transition matrix of u kinetic important coarse-grained states and $\tilde{\mathbf{\Pi}} = \mathrm{diag}(\tilde{\pi}_1, ..., \tilde{\pi}_u)$ contains the corresponding stationary distribution of the coarse-grained u-state HMM. χ is a matrix, whose elements $\chi_{Ij} \in \mathbb{R}^{u\times v}$ hold the probability to observe a macrostate I, while the system is in microstate j. $\mathbf{\Pi} = \mathrm{diag}(\pi_1, ..., \pi_v)$ is the stationary distribution of the v-state MSM.

To calculate a coarse-grained matrix, the microstates are grouped into a membership matrix $\mathbf{B} \in \mathbb{R}^{v\times u}$, the elements of which contain the probability that a microstate i participates in a macrostate J and are computed by linear transformation of the first u eigenvectors λ_i (PCCA+ and PCCA++ methods). χ is then calculated as

$$\chi = \tilde{\mathbf{\Pi}}^{-1}\mathbf{B}^{\mathrm{T}}\mathbf{\Pi}. \tag{7}$$

Also the $u \times u$ transition matrix of Eq.6 can be calculated from the membership matrix $\mathbf{B}$ as

$$\tilde{\mathbf{P}} = (\mathbf{B}^{\mathrm{T}}\mathbf{B})\mathbf{B}^{\mathrm{T}}\mathbf{P}\mathbf{B}, \tag{8}$$

where $\mathbf{P}$ is the $v \times v$ MSM transition matrix. Together with Eq.7, Eq.8 is used to estimate the HMM.

A transition rate matrix $\mathbf{K}$ can then be derived, which describes the state transitions in terms of the actual kinetics. The relation between the rate and probability matrix is given by the equation

$$\tilde{\mathbf{P}}(\tau) = \exp(\tau\mathbf{K}), \tag{9}$$

where τ is here again the lag time at which the given HMM is constructed.

Let us now consider a multistate receptor that permits significant ligand access to only a single accessible state r, as described previously [15]. In a regime where ligand binding is limited by conformational gating to r and not by a subsequent induced fit association rate constant (k^{if}), the overall bimolecular association rate constant (k_{on}) is dominated by the gated association rate constant (k^{g}) and can be expressed as:

$$\mathrm{k}_{on} \sim \mathrm{k}^{g} = \gamma\mathrm{k}^{ug}, \tag{10}$$

where γ=$\mathrm{k}_{acc}/(\mathrm{k}_{acc}$+$\mathrm{k}_{nacc})$, is the conformational gating factor and represents the probability of the ligand finding the apo-receptor in state r. The first-order rate constants k_{acc}=$\sum_{i\neq r}\mathrm{k}_{ir}$ and k_{nacc}=$\sum_{j\neq r}\mathrm{k}_{rj}$ describe the overall transition kinetics between accessible state r and all other non-accessible states in the apo-receptor. Here, k_{ij} represent the (off-diagonal) elements of the transition rate matrix $\mathbf{K}$, representing the net flux from a single metastable state i to another metastable state j, and which can be computed directly from the HMM of the apo-receptor, as described above.

We now expand this model more generally to the case of multiple accessible states. The apo-state space is divided into two disjoint subsets, containing all non-accessible N and all accessible M states. The first-order conformational rate constants between

bioRxiv preprint doi: https://doi.org/10.1101/2021.06.22.449380; this version posted June 23, 2021. The copyright holder for this preprint (which was not certified by peer review) is the author/funder, who has granted bioRxiv a license to display the preprint in perpetuity. It is made available under aCC-BY-NC-ND 4.0 International license.

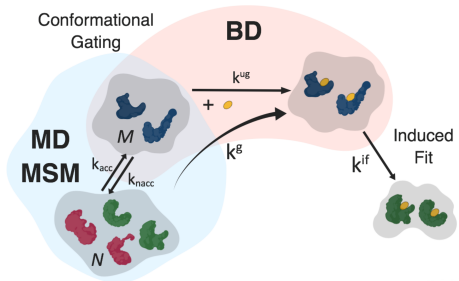

Fig 2. Schematic of coupling approach between BD and MD/MSM to compute gated ligand binding to accessible states of a multiconformation receptor. A conformational gating factor (γ), representing the probability of accessing the accessible states is derived from the previously described hidden Markov model (HMM) transition matrix of the apo-state conformational kinetics (see Theory), where γ=$\mathrm{k}_{acc}/(\mathrm{k}_{acc}+\mathrm{k}_{nacc})$ and where k_{acc} and k_{nacc} are the first-order rate constants for transitioning into the accessible and non-accessible states, respectively. BD simulations are then performed for binding to the accessible states yielding a second-order ungated association rate constant (k^{ug}). For ligand-receptor complexes in which the subsequent induced fit step (k^{if}) to form a closed bound complex is not rate-limiting, the overall association kinetics can be approximated by a gated rate constant, k^{g}=$\gamma\mathrm{k}^{ug}$.

the two sets of states can then be expressed as the sum of transition rates from non-accessible $n \in N$ to accessible $m \in M$ states such that $\mathrm{k}_{acc} = \sum \mathrm{k}_{nm}$ and vice versa $\mathrm{k}_{nacc} = \sum \mathrm{k}_{mn}$. A gating factor ($\gamma$) can then be defined for the overall transition of the accessible states:

$$\gamma = \frac{\sum_{N,M} \mathrm{k}_{nm}}{\sum_{N,M} (\mathrm{k}_{mn} + \mathrm{k}_{nm})}. \tag{11}$$

However, γ alone does not contain the information about the respective contributions of the accessible states. To account for these we define the state specific gating factor $\Gamma_m = \gamma\epsilon_m$, where ϵ_m represents the relative population of state $m \in M$ and which can also be computed from the HMM. By combining with ungated rate constants (k_m^{ug}) computed from BD simulations for each state m, the overall gated association rate constant (k^g) for the set of states, M, is then given by:

$$\mathrm{k}^g = \sum_M \Gamma_m \cdot \mathrm{k}_m^{ug} \tag{12}$$

$$= \gamma \sum_M \epsilon_m \cdot \mathrm{k}_m^{ug}. \tag{13}$$

With this formalism, the combined ungated rate constant (k^{ug}) for the set of states, M, is then given by:

$$\mathrm{k}^{ug} = \sum_M \epsilon_m \cdot \mathrm{k}_m^{ug}, \tag{14}$$

and in the limiting case where there is only one accessible metastable state, $\epsilon_m = 1$, we recover the single-state gating factor. Extending the previous formalism [15] to multiple accessible states, 'slow' and 'fast' gating regimes can be differentiated in relation to the characteristic diffusion time $\tau_d = r_c^2/D$, where r_c is the collision distance between the molecules and D is the relative translational diffusion constant by:

bioRxiv preprint doi: https://doi.org/10.1101/2021.06.22.449380; this version posted June 23, 2021. The copyright holder for this preprint (which was not certified by peer review) is the author/funder, who has granted bioRxiv a license to display the preprint in perpetuity. It is made available under aCC-BY-NC-ND 4.0 International license.

$$\mathrm{k}^g = \gamma \sum_M \epsilon_m \cdot \mathrm{k}_m^{ug}, \tau_c >> \tau_d \tag{15}$$

$$\mathrm{k}^g = \sum_M \epsilon_m \cdot \mathrm{k}_m^{ug}, \tau_c << \tau_d, \tag{16}$$

where τ_c is the characteristic timescale of conformational gating given by:

$$\tau_c = \frac{1}{\sum_{N,M}(\mathrm{k}_{mn} + \mathrm{k}_{nm})}. \tag{17}$$

Materials and Methods

Initial preparation

Atomic coordinates for wildtype dimeric HIV-1 protease in the semi-open conformation were extracted from the 1HHP crystal structure [77] in the Protein Data Bank [93]. Those for a wide-open conformation were taken from the reported structure in our previous study [86]. The standard AMBER forcefield (ff03) [94] was used to describe all protease parameters. A dianionic state was assigned to the catalytic dyad as, at physiological pH, the unbound protease is unprotonated, whilst mono-protonation is thought to occur upon or after ligand binding [95–98]. The VMD software package [99] and the LEAP module of the AMBER 16 software package [100] then used to build the initial systems. Each system was solvated using atomistic TIP3P water [101] in a cubic box extending at least 7 Å around the complex and then electrically neutralised with an ionic concentration of 0.15 M NaCl, resulting in fully atomistic systems for both semi-open and wide-open conformations of ∼40,000 atoms.

Equilibration and production MD simulations

All equilibration and production simulations were performed using ACEMD [102]. During equilibration the positions of the heavy protein atoms were restrained by a 10 kcal/mol/Å^2 spring constant and conjugate-gradient minimisation was performed for 2000 steps. The hydrogen atoms and water molecules were then unrestrained and allowed to evolve for a total of 500 ps at 300 K in the NVT ensemble to ensure thorough solvation of the complex and to prevent premature flap collapse [103]. The magnitude of the restraining spring constant was set to 1 kcal/mol/Å^2 for the following 500 ps, then to 0.05 kcal/mol/Å^2 for 500 ps, then finally to zero for 500 ps. The temperature was maintained at 300 K using a Langevin thermostat with a low damping constant of 0.1/ps and the pressure was maintained at 1 atm using a Nose-Hoover barostat. The sytem was finally equilibrated for 6 ns of unrestrained simulation in the isothermal-isobaric ensemble (NPT). The long range Coulomb interaction was handled using a GPU implemention [104] of the particle mesh Ewald summation method (PME) [105] with grid size 84x84x84. A non-bonded cut-off distance of 9 Å was used with a switching distance of 7.5 Å. For the equilibration runs, the SHAKE algorithm [106] was employed on all atoms covalently bonded to a hydrogen atom with an integration timestep of 2 fs. Production simulations took place in the NVT ensemble. The hydrogen mass repartitioning scheme [107] was used, allowing a timestep of 4 fs. All other parameters were kept the same as the equilibration phase. The production data set consisted of 465 and 499 simulations started from semi-open and wide-open conformations respectively, each for 130 ns with coordinate generation every 100 ps.

Our molecular simulation protocol for the HIV-1 protease has been previously validated using NMR S^2 order parameters [86].

bioRxiv preprint doi: https://doi.org/10.1101/2021.06.22.449380; this version posted June 23, 2021. The copyright holder for this preprint (which was not certified by peer review) is the author/funder, who has granted bioRxiv a license to display the preprint in perpetuity. It is made available under aCC-BY-NC-ND 4.0 International license.

Determination of collective variable space

Before MSMs can be constructed from MD simulation data, the high-dimensional configuration space of atomistic coordinates needs to be projected onto a low-dimensional, but meaningful, collective-variable (CV) space. Finding the appropriate CV space is still a major challenge, despite considerable efforts at systemisation [54–56]. A minimum fluctuation alignment (MFA) method, introduced previously [44] and developed further here, was used to determine a set of information-rich collective variables that describe flap conformations in HIV-1 PR.

Minimum fluctuating (MF) residues for the protease were identified as residues 23, 24, 85 and 89-92 of each monomer. The homodimeric C_2 symmetry of the protease makes identical MF residue subsets on both monomers a sensible choice of vector termini. The x-axis was thus chosen to be the vector between the center of mass (COM) of the backbone atoms of residues 89-92 of the second and first monomers respectively. A second vector was selected (between the COM of residues 23,24 and 85 of each monomer respectively). The resultant z-axis therefore approximated the C_2 symmetry axis. The selected residues are either within the α-helix of the protease or within the β-sheet region that supports each side of the active-site and thus exhibit minimal RMSFs compared to other residues [86]. Due to the choice of the x-axis, the resultant y-axis was similar to the vector describing the binding conduit of bound peptides in the active site [70, 71].

A 3D metric based on the re-aligned cylindrical polar components of the I50-I50′ C_α-atom flap tip separation vector, $\lambda(\lambda_r, \lambda_\Theta, \lambda_z)$, was then devised. A wrapping angle of 50° was added to all values of λ_Θ with a wrapping modulus of 360°. This extends the original 1D Cartesian λ_x metric used earlier [44] and was employed as a set of collective variables to describe the conformational transitions of the system.

Markov state model

The software package pyEMMA2 [92] was used for Markov state model construction and analysis. The 3D λ-space was used as the set of collective variables in which to construct the models. The data were subsequently clustered into 100 microstates using k-means clustering in this 3D CV-space. Discretized state labels were assigned and Markov state models (MSMs) with Bayesian error estimation were built at various lag-times (τ) and the computed relaxation timescales analyzed as a function of τ. Constant relaxation timescales for the slowest transitions were exhibited at τ= 30 ns, significantly shorter than the length of all trajectories used, with time scale separation suggesting a set of five kinetically distinct macrostates (C1-C5). A subsequent MSM was then estimated using a lag time of 30 ns. The 100-state MSM at τ= 30 ns was coarse-grained into a five-state hidden Markov model (HMM) and validated using a generalized Chapman-Kolmogorov test. Fuzzy clustering of microstates into macrostates was performed and the resulting membership ($\mathbf{B}$) and observation (χ) distribution matrices computed. The transition matrix ($\tilde{\mathbf{P}}$) between a smaller set of meaningful macrostates was then computed using Equations 7 and 8. The stationary distribution of the five states and the transition kinetics between these states was then extracted from the HMM.

Structural characterization

Representative snapshots of the kinetically distinct macrostates (C1-C5) were extracted for structural characterization. Macrostate C1 was noted to be an antisymmetric doublet-state (see Results), thus representative structures were extracted separately for each of the corresponding substates C1a and C1b. For each macrostate, the microstate with the largest observation probability was selected. Within each corresponding microstate, conformers were ranked in order of proximity in the λ-space to the centroid

bioRxiv preprint doi: https://doi.org/10.1101/2021.06.22.449380; this version posted June 23, 2021. The copyright holder for this preprint (which was not certified by peer review) is the author/funder, who has granted bioRxiv a license to display the preprint in perpetuity. It is made available under aCC-BY-NC-ND 4.0 International license.

and the closest 1000 conformers extracted for analysis. Microstates for C1a and C1b corresponded to those with the first and second highest observation probability, respectively, for macrostate C1. In addition, various structural features from the extracted ensembles were compared with respect to the first replica of a previous ensemble MD simulation of the HIV-1 protease in a closed conformation and bound to the SP1-NC natural octapeptide [108,109]. Analysis was implemented using Python scripts based on the MDAnalysis toolkit [110]. Distributions of the root-mean-squared-deviations (RMSDs) of the C_α backbone with respect to semi-open (1HHP) and closed (1KJ7) reference crystal structures were computed as were the distributions of the absolute flap-tip separation (λ). Instantaneous hydrogen bonds were computed based on a donor-acceptor distance threshold of $\leq$3.5 Å and a donor-hydrogen-acceptor angle of $\geq$150°. Only those hydrogen bonds with an exhibition frequency $f_{hb} \geq 0.5$ were considered stable - the corresponding mean distances and angles were computed from the exhibited snapshots. Hydrophobic contacts were determined from sidechain-sidechain distance analysis; the minimum non-hydrogen atom distance between pairs of sidechains was computed for each conformer. A hydrophobic contact was assigned to hydrophobic residue pairs with a mean minimum distance $\leq$ 5 Å across the corresponding ensemble/trajectory. Volumetric maps of the averaged weighted atomic densities for each apo-conformer ensemble and the natural octapeptide from a former study [108] were computed with the Volmap tool in VMD [99] using a grid spacing of 0.5 Å.

Brownian dynamics simulations

Atomistic coordinates for the 100 conformers most proximal to the microstate centroid in each structural ensemble were extracted to use in Brownian dynamics (BD) simulations to compute diffusional association rate constants for a set of inhibitors with experimentally determined rate constants [88]. Protein partial atomic charges were assigned using the ff14SB forcefield [111]. Atomistic coordinates and partial charges for the inhibitors were extracted from a previous study [112]. PQR files were generated using the PDB2PQR module in AMBER18 [113]. Electrostatic potential grids for the protein structures and for the inhibitors were computed using APBS [114] with a grid spacing of 1 Å, an ionic concentration of 150 mM and a temperature of 298K, corresponding to experimental conditions, as well as a solvent dielectric constant of 78, a solute dielectric constant of 2 and an ionic radius of 1.5 Å. For the calculation of the electrostatic potential, the linearized Poisson-Boltzmann equation was solved under the single Debye-Hückel dielectric boundary condition. All BD simulations were carried out using SDA7.2.3 [115], and association rates constants were computed using the Northrup-Allison-McCammon algorithm [23]. SDA employs an effective charge model (ECM) [116], where the charge on a reduced number of centers is fitted to reproduce, in a uniform dielectric medium, the potential computed with APBS for a heterogeneous dielectric medium in the region around the molecule. ECM charges for the protein were determined using the standard protocol in SDA, those for the ligands were determined from a newly developed protocol [117]. Electrostatic and hydrophobic desolvation grids were generated with a grid spacing of 1 Å. The ionic strength was set to zero for computing the electrostatic grid, with electrostatic and hydrophobic desolvation factors of 0.36 and -0.013 assigned, respectively. The solute and probe radii were both set to 1.4 Å.

Translational and rotational diffusion coefficients were calculated for all solutes using Hydropro [118] with an atomic element radius (AER) of 2.9 Å and 1.2 Å for protein and ligands respectively, with a σ_{min} of 1.0 Å and a σ_{max} of 2.0 Å. For each macrostate-ligand combination, a diffusional association rate constant was computed from a set of 100000 trajectories (100 protein conformers $\times$ 1000 replicas). Each trajectory was started with an initial center-to-center distance of 150 Å between the solutes and stopped

bioRxiv preprint doi: https://doi.org/10.1101/2021.06.22.449380; this version posted June 23, 2021. The copyright holder for this preprint (which was not certified by peer review) is the author/funder, who has granted bioRxiv a license to display the preprint in perpetuity. It is made available under aCC-BY-NC-ND 4.0 International license.

when the solutes reached a seperation of 250 Å. A variable time step was used, linearly ranging from 1 ps at a solute-solute separation of 50 Å to 20 ps at a separation of 90 Å. A distance threshold of 3 Å was set for pairs of contacts to be assigned as independent reaction criteria that described formation of a receptor-ligand encounter complex. Reaction criteria included polar interactions at 3.5 Å defined in terms of acceptor-donor pairs, as well as methyl, halogen and aromatic interactions at 4.5 Å, defined in terms of π-π pairs from the above-mentioned crystal structures of the corresponding complexes, filtering out any residues that did not match the sequence of the apo-protein (PDB: 1HHP) and including symmetrically equivalent contacts due to the C_2 symmetry of the protease dimer. Reaction criteria coordinates were taken for each BD simulation after superimposition of the C_α backbone of residues 1-43 and 58-99 in each monomer of a given apo-conformer with the corresponding original inhibitor-bound complex. An encounter complex was counted whenever a sufficient number of contacts from the subset of pre-defined reaction criteria was observed within a specified distance. The association rate constant was initially calculated using a range of definitions of encounter complex in terms of number of contacts, $\{1, ..., 5\}$ and their corresponding distances from a minimum of 3 Å and with increasing window intervals of 0.5 Å up to 20 Å. Ungated association rate constants were subsequently computed by requiring the formation of 3 independent contacts shorter than 4 Å.

BD docking simulations were performed for each of the ligands diffusing to each of the protein macrostates under the same reaction criteria as for the association rate calculations to check if the reaction criteria corresponded to ligands binding within the active site of the protease. 10000 trajectories were run for protein conformers with the highest number of encounters obtained in the association rate constant calculation simulations, and complexes were recorded at a 4 Å reaction criterion window distance.

Results

Ensemble molecular dynamics simulations resulted in $\sim 1.25 \times 10^6$ molecular conformers for subsequent analysis. In order to reveal and characterize meaningful conformational states from this ensemble, we constructed a converged Markov state model (MSM) based on a suitable projection of the atomistic coordinates into a three-dimensional collective variable space. This enabled us to identify a small set of discretised macrostates of the system, compute their equilibrium distribution and transition kinetics, and then analyse representative constituent conformers belonging to each macrostate to reveal distinct structural features. This in turn allowed the differentiation of the macrostates that were accessible and non-accessible to ligand binding and the subsequent computation of a gating factor. Brownian dynamics simulations enabled computation of the ungated association rate constant to accessible states from which the overall gated rate constant could be computed for a set of ligands.

Kinetic network of HIV-1 protease conformations

The 3D λ-state-space in cylindrical polar coordinates (λ_r, λ_Θ, λ_z) was chosen as a collective variable space in which to construct Markov state models (MSMs). The λ-state-space was discretised into 100 microstates. MSMs constructed using Bayesian error estimation across a range of lag-times (τ) show independence of the relaxation timescale (t_n) for the slowest-order transitions at $\tau = 30$ ns (Figure 3(a)) and a significant timescale separation between the fourth and fifth non-stationary eigenvectors with $t_4/t_5 > 2$ (Figure 3(b)).

bioRxiv preprint doi: https://doi.org/10.1101/2021.06.22.449380; this version posted June 23, 2021. The copyright holder for this preprint (which was not certified by peer review) is the author/funder, who has granted bioRxiv a license to display the preprint in perpetuity. It is made available under aCC-BY-NC-ND 4.0 International license.

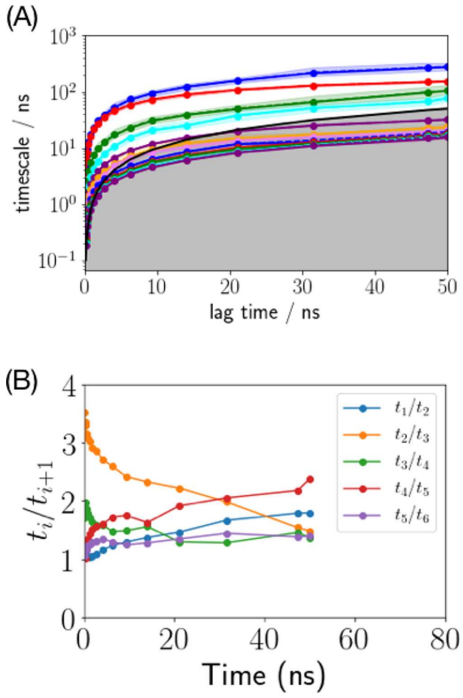

Fig 3. (a) Relaxation timescales (t_n) for the dominant non-stationary eignvectors of the MSMs constructed in the λ-space at increasing lag times (τ) with Bayesian error estimation. Independence of the relaxation timescale with lag time is observed at $\tau =$ 30 ns. (b) Plot of the ratio of proximal relaxation timescales (t_i/t_{i+1}) shows a signifcant timescale separation of $t_4/t_5 > 2$ at $\tau = 30$ ns suggesting the existence of five kinetically meaningful metastable states.

bioRxiv preprint doi: https://doi.org/10.1101/2021.06.22.449380; this version posted June 23, 2021. The copyright holder for this preprint (which was not certified by peer review) is the author/funder, who has granted bioRxiv a license to display the preprint in perpetuity. It is made available under aCC-BY-NC-ND 4.0 International license.

Consequently a MSM was constructed with Bayesian error estimation using 100 microstates and τ = 30 ns and the microstate equilibrium distribution computed. A potential of mean force (PMF) landscape, computed for 2D projections of the λ-state-space and weighted by this equilibrium distribution (Figure 4(A)), samples a large region, ranging from $0 < \lambda_r < 40$ Å, $0 < \lambda_\Theta < 360$ Å and $-15 < \lambda_z < 15$ Å. This PMF differentiates several significant energetic minima with $\lambda(\lambda_r, \lambda_\Theta, \lambda_z)$ centers at $\lambda \sim$(8,40,$\pm$5) Å, $\lambda \sim$(5,100,0) Å, $\lambda \sim$(20,150,0) Å and $\lambda \sim$(8,300,0) Å, with minima values of -0.5, -4.5, -3.5 and -2.5 kcal/mol respectively.

Timescale separation analysis implies that five kinetically meaningful macrostates exist, with the two slowest transitions in the system being around or larger than the 100 ns-timescale. Based on this a corresponding five-state coarse-grained hidden Markov model (HMM) was computed. This further clustered the microstates into kinetically separated macrostates, C1-C5 (Figure 4(A)). This model was validated by performing a generalized Chapman-Kolmogorov (C-K) test (Supporting Figure S1(A)). The C-K test showed good agreement with the predicted probability decay from the model at τ = 30 ns ($\mathrm{p}_{IJ}^{k}(\tau)$) and the expected decay from models constructed at multiple (k) lag times ($\mathrm{p}_{IJ}(k\tau)$). Moreover, the probabilities, χ, of observing each of the 100 microstates across the five macrostates (see Theory) were computed and projected onto the λ-space (Supporting Figure S1(B)). This analysis confirmed that the five macrostates also exhibited mutual exclusivity of microstate probabilities and therefore could be interpreted as distinct states. The microstates that constitute most macrostates correspond well with the energetic minima in the PMF. The only exception is C2, whose microstates seem to be primarily distributed in a transitional region between C4 and C5.

The HMM yielded a kinetic network of the stationary distributions and their respective first-order transition kinetics (Figure 4(B)). The five states, C1-C5, exhibit different stationary probabilities (ρ) with $\rho_1 = 0.1$, $\rho_2 = 0.29$, $\rho_3 = 0.07$, $\rho_4 = 0.25$ and $\rho_5 = 0.29$ corresponding to zero-centered Boltzmann-weighted free energies of $\sim$-0.2, -0.8, 0, -0.7 and -0.8 kcal/mol, respectively. Thus the free energy differences betwen all five states are thermodynamically barely indistinguishable from thermal noise ($\sim$0.6 kcal/mol).

Nonetheless, there are significant differences in the transition kinetics between the various states. Only direct fluxes faster than 100 μs are shown ($\geq 3\times10^{-4}/\tau = 0.01$ $\mu\mathrm{s}^{-1}$). Forward and reverse transitions between C2 and C5, as well as between C2 and C4, are well within the sub-μs timescale (> 1 $\mu\mathrm{s}^{-1}$), although the rate for direct transition between C4 and C5 is $\sim$0.1 $\mu\mathrm{s}^{-1}$. The C1 conformation only directly accesses the C4 conformation, and does so with kinetics slower than the μs-timescale, whilst the C3 conformation accesses both C2 and C4 conformations with forward and reverse kinetics faster and slower than 1 $\mu\mathrm{s}^{-1}$, respectively. Only the C4 conformation directly accesses all other conformations on a timescale faster than 100 μs.

Structural characterization of principal conformations

The conformational features of representative structures corresponding to each of the macrostates were analyzed. Probabilistic clustering of microstates into macrostates via the observation probability matrix ($\chi_{I,j}$) enables selection of the most likely microstates that represent each macrostate (Supporting Table S1). For each macrostate, the most probable microstate largely coincides with the corresponding minimum or minima in the λ-space (Supporting Figure S2). Macrostate C1 is characterized by two distinct minima in the λ-space equidistantly separated from the origin along λ-z. This implies a symmetry-related doublet state. Moreover the two most probable microstates for C1 correspond to each of these minima - thus C1 was split into two sub-states, C1a and C1b, in subsequent analyses corresponding to the $+\lambda_z$ and $-\lambda_z$ regions respectively. A set of 1000 closest conformers was thus extracted from the most probable microstate of each macrostate based on the ranked proximity of each snapshot to the corresponding

bioRxiv preprint doi: https://doi.org/10.1101/2021.06.22.449380; this version posted June 23, 2021. The copyright holder for this preprint (which was not certified by peer review) is the author/funder, who has granted bioRxiv a license to display the preprint in perpetuity. It is made available under aCC-BY-NC-ND 4.0 International license.

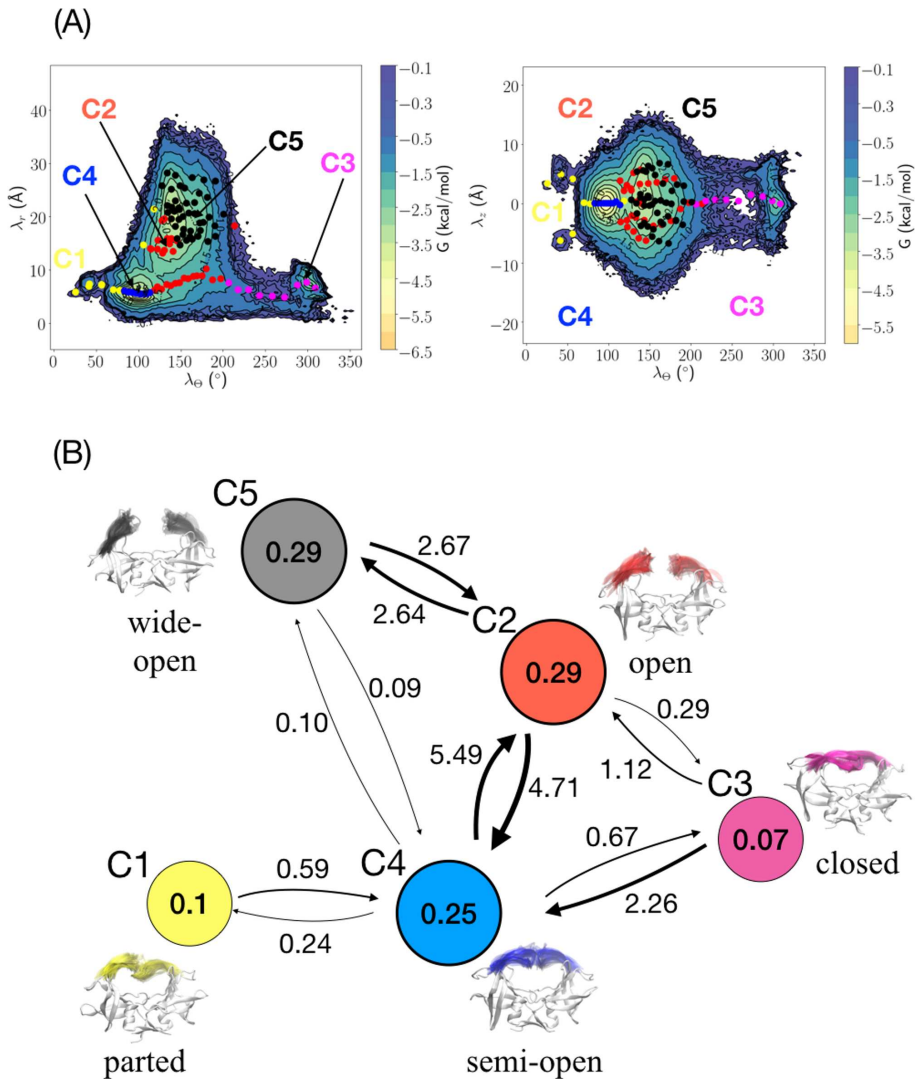

Fig 4. (A) Potential of mean force (PMF) of HIV-1 PR in the apo-state in the $\lambda(\lambda_r,\lambda_\Theta,\lambda_z)$-collective variable space, projected onto λ_r-λ_Θ and λ_Θ-λ_z. Values are in kcal/mol. Energetic minima correspond to frequently sampled regions of the λ-space weighted by the equilibrium distribution of discretised microstates of the MSM. A HMM based on five macrostates (C1-C5) has clusters of corresponding microstates whose λ-centroids are overlayed on the PMF. (B) Kinetic network between the five coarse-grained macrostates, corresponding to conformations C1-C5, determined by the hidden Markov model (HMM). Stationary probabilities are shown in the circles, forward and reverse first order transition kinetics are shown by arrows with values in μs^{-1}. Displayed structures for each macrostate are superpositions of conformers belonging to the most probable microstate given the corresponding macrostate.

bioRxiv preprint doi: https://doi.org/10.1101/2021.06.22.449380; this version posted June 23, 2021. The copyright holder for this preprint (which was not certified by peer review) is the author/funder, who has granted bioRxiv a license to display the preprint in perpetuity. It is made available under aCC-BY-NC-ND 4.0 International license.

microstate centroid in the 3D cylindrical polar λ-space.

Visual inspection of each set of conformers reveals that several macrostates correspond to known conformations of HIV-1 protease (Figure 4(B)), as well as a previously unidentified conformation. Hydrogen bonds and sidechain-sidechain contacts between each flap and the opposite (*trans*) monomer were analyzed (Supporting Tables S2 and S3). C2 and C5 correspond to open and wide-open conformations, respectively, where the flaps are pulled back enabling sterically unhindered access to the active site (Figure 4(B)). These two conformations exhibit no *trans* flap-monomer interactions. Macrostates C3 and C4 correspond to the characteristic closed and semi-open conformations, respectively, where the flaps extend over the active site but with opposite handedness (Figure 5 and Figure 6(A)-(B)). In C3, the I50 sidechain interacts with the characteristic array of hydrophobic residues (V32′, I47′, I54′, I80′ and I84′) on the opposite monomer and symmetrically vice versa. In C4, these contacts are missing, and are instead replaced predominantly a smaller set of hydrophobic contacts (I50-I50′,I50-F53′ and F53-I50′) and a symmetric pair of inter-glycine amide hydrogen bonds (G51–N-H–O-G49′ and G51′–N-H–O-G49). C1a and C1b are identified as anti-symmetric sub-states of a novel conformation, where one flap is extended as in the semi-open conformation whilst the other orients under it and traverses across the active site towards the other monomer (Figure 5). They share a subset of hydrophobic contacts with both C3 (C1a: I50-V32′ and I50-I47′, C1b: V32-I50′ and I47-I50′) and C4 (C1a: F53-I50′, C1b: I50-F53′) but also exhibit sidechain contacts (C1a: I50-D30′ and M46-I50′, C1b: D30-I50′ and I50-M46′) and a backbone hydrogen bond (C1a: G48′-N-H–O-I50, C1b: G48-N-H–O-I50′) that are unique to them and which serve to stabilise these conformations. In particular, the I50-D30′/D30-I50′ contacts bring the corresponding flap tip diagonally across to the opposite side of the active site.

Observation of C3 and C4 are further confirmed by unimodal distributions of flap-RMSD with respect to crystal-structures of closed and semi-open conformations for which C3 and C4 exhibit the smallest mean RMSDs, 1.8±0.5 Å and 2.0±0.4 Å, respectively (Figure 6(C)). All other macrostates exhibit significantly larger mean RMSDs with respect to both crystal structures. Analysis of the distribution of absolute flap tip separation distances (λ) shows that C3 and C4 all exhibit peak distances substantially lower than 10 Å, whilst C1a and C1b both peak at ∼10 Å(Figure 6(D)). By contrast, C2 and C5 exhibit a relatively broad distribution of distances peaking at 15 Å and 20 Å respectively, implying that only these two states provide sufficient access to peptidomimetic ligands binding in the active site. The λ-distributions of all conformers for each of the top microstates of every macrostate exhibit very similar profiles respectively to the macrostate conformer sets selected here (Supporting Figure S2).

Cross-sections of averaged weighted atomic density over the conformers of each set provide further insight into the steric active-site accessibility of the corresponding macrostates (Figure 6(E)-(H)). The averaged density of a closed bound reference complex of HIV-1 protease with the SP1-NC cleavage peptide was calculated based on previous simulations [108, 109]. Superimposing densities calculated individually for the apo-protease (gray) and ligand (red) from this complex are consistent with both a snugness of fit and the inaccessibility of binding the enzymatically viable closed conformation (Supporting Figure S3). The ligand exhibits significant density between -5 Å $< x <$ 5Å, -15 Å $< y <$ 15Å, 5 Å $< z <$10 Å. To provide corresponding steric context to the macrostates, the density of the peptide from this analysis was superimposed with those calculated from each of the representative conformer sets. Cross-sections in the x-y plane reveal that at z = 8 Å, states C1a, C1b and C3 exhibit partial occlusion at the edges of the active site, whilst states C2, C4 and C5 exhibit a zero-density lateral exit pathway in the y-direction. Moreover, states C2-C5 exhibit a zero-density groove corresponding to the active site that can accommodate the reference peptide density.

bioRxiv preprint doi: https://doi.org/10.1101/2021.06.22.449380; this version posted June 23, 2021. The copyright holder for this preprint (which was not certified by peer review) is the author/funder, who has granted bioRxiv a license to display the preprint in perpetuity. It is made available under aCC-BY-NC-ND 4.0 International license.

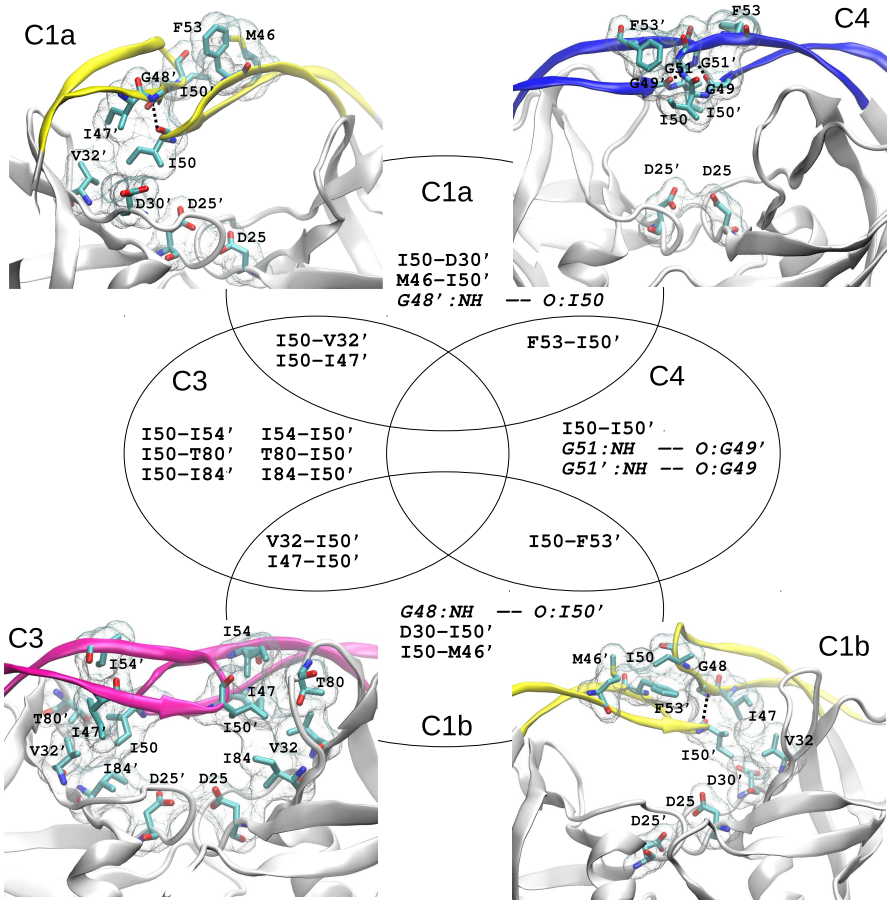

Fig 5. Mututally exclusive and shared sidechain-sidechain and hydrogen bond interactions between each flap region and the alternate monomer across different macrostates. C2 and C5 do not form any such interactions and are not displayed. Hydrogen bonds are marked with dashed black lines and noted in italics. The catalytic dyad D25/D25′ is shown for structural context.

bioRxiv preprint doi: https://doi.org/10.1101/2021.06.22.449380; this version posted June 23, 2021. The copyright holder for this preprint (which was not certified by peer review) is the author/funder, who has granted bioRxiv a license to display the preprint in perpetuity. It is made available under aCC-BY-NC-ND 4.0 International license.

However, by z = 12 Å, only macrostates C2 and C5 maintain this groove, whilst the flap extensions in the other conformations incur protein density that closes off peptide escape in the z-direction. Lateral cross-sections in the x-z and y-z planes confirm that only the C2 and C5 macrostates maintain a zero-density pathway out of the active site along the z-direction. Thus, combining exit pathways from the y- and z-directions, only macrostates C2, C4 and C5, corresponding to open, semi-open and wide-open conformations, respectively are selected as ligand accessible states for rigid body binding simulations.

Gated ligand binding of peptidomimetic inhibitors

A set of peptidomimetic ligands (Figure 7), covering a range of experimentally determined association rate constants, k_{on} $\sim 10^4$ - 10^{10} $\mathrm{M}^{-1}\mathrm{s}^{-1}$, were chosen for Brownian dynamics simulations to each of the three chosen (C2, C4 and C5) accessible states of HIV-1 protease. The closest 100 conformers to the centroid of the most probable microstate were extracted for each of the accessible states. All three sets of conformers exhibit similar translational diffusion constants ($< D_T(C2) > = 9.90 \pm 0.08 \times 10^{-11}$ m^2/s, $< D_T(C4) > = 1.00 \pm 0.01 \times 10^{-10}$ m^2/s), $< D_T(C5) > = 9.80 \pm 0.08 \times 10^{-11}$ m^2/s) and similar radii of gyration ($r_g(C2) = 1.99 \pm 0.03 \times 10^{-9}$ m, $r_g(C4) = 1.91 \pm 0.02 \times 10^{-9}$ m, $r_g(C5) = 2.04 \pm 0.02 \times 10^{-9}$ m). Translation diffusion constants and radii of gyration for the ligands range between 2.88 - 4.58 $\times 10^{-10}$ m^2/s and 4.43 - 7.83 $\times 10^{-10}$ m, respectively, yielding a characteristic diffusional timescale, τ_d, that ranges between $\sim$ 12 - 16 ns depending on the ligand. By contrast, based on the outcome of the MSM and using Equation 17, the characteristic protein conformational transition timescale, τ_c, is computed to be almost an order of magnitude larger (τ_c = 85 ns), suggesting a 'slow' gating regime ($\tau_c >> \tau_d$). Thus, there is a kinetic gating factor to binding and via Equation 11, this is computed to be $\gamma = 0.75$.

Ungated rate constants (k_m^{ug}) were then computed from BD simulations to each of the macrostates m=C2,C4 and C5, where the value for each state was computed using ensemble averaging over the set of 100 conformers that represented it. For each state, a number of complexes were formed at the reaction criteria corresponding to the bound state (see Methods). BD docking simulations were performed for each of the ligands binding to each of the accessible protein macrostates under these reaction criteria and the most popular clusters inspected. These confirmed that fulfillment of the reaction criteria corresponds to ligands binding within the active site of the protease (Supporting Figure S4). Similarly, BD simulations were carried out for ligands binding to the inaccessible states (C1 and C3). Lack of complexes formed within the active site of these two states thus further confirmed assignment of them as inaccessible (Supporting Figure S4).

Values for the ungated rate constants (k_m^{ug}) were combined to give the overall ungated rate constants for the set of accessible states (k^{ug}) and finally multiplied by the gating factor γ to obtain the gated rate constants (k^{g}). Our calculations show, as expected, that binding to the C4 (semi-open) state is slower than to the C2 (open) state and also slower than binding to the C5 (wide-open) state for all ligands except Nelfinavir and Saquinavir (Table 1). Furthermore, binding for most ligands is faster to C2 than C5, occasionally by several-fold, whilst for Ritonavir and B376 it is only marginally slower. The resulting combined ungated rate constants (k^{ug}) are almost all within one order of magnitude of each other, ranging from $k^{ug}\sim$60-750 $\mu\mathrm{M}^{-1}\mathrm{s}^{-1}$ and, as the gating factor is 0.75, the gated rate constant range is only marginally reduced ($k^g\sim$45-565 $\mu\mathrm{M}^{-1}\mathrm{s}^{-1}$). This results in k^g being up to several orders faster than the corresponding experimental association rate constants (k_{on}^{exp}) for most ligands, similar for B376, and several orders of magnitude slower for the fastest binder, DMP323 (Table 1).

bioRxiv preprint doi: https://doi.org/10.1101/2021.06.22.449380; this version posted June 23, 2021. The copyright holder for this preprint (which was not certified by peer review) is the author/funder, who has granted bioRxiv a license to display the preprint in perpetuity. It is made available under aCC-BY-NC-ND 4.0 International license.

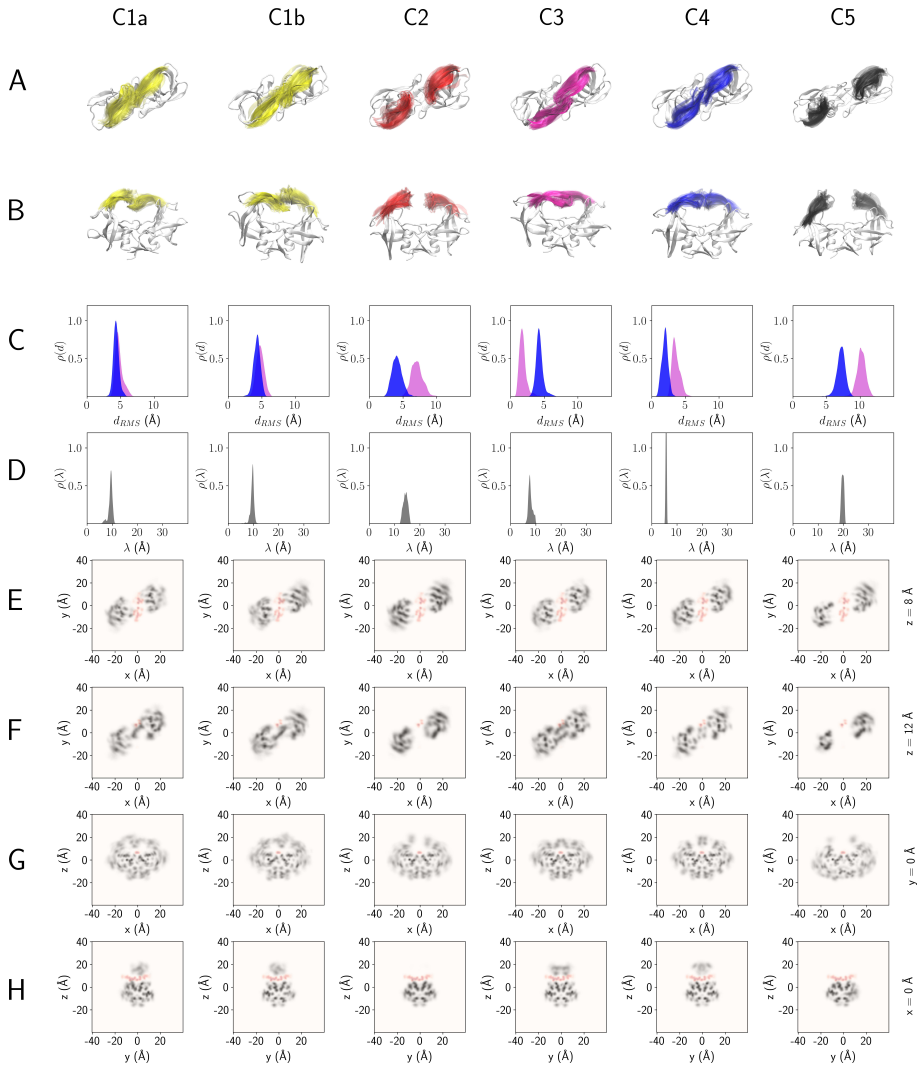

Fig 6. Structural characterization of representative conformers of each macrostate of HIV-1 apo-protease. (A) Top (x-y plane) and (B) side (x-z plane) views of ribbon representations of superimposed structures in each conformational ensemble, (C) Distribution ($\rho(d)$) of root-mean-square deviations (d_{rms}) of C_α atoms of protease flaps (residues 43-58 in each monomer) with respect to crystallographic reference closed (pink) and semi-open (blue) structures. (D) Distribution of ($\rho(\lambda)$), the absolute flap tip separation distance (λ). (E-H) Cross-sections of superimposed volumetric density between the SP1-NC natural peptide in a closed-bound reference structure (red) and representative conformational ensembles of each macrostate (grey) in the x-y plane at z =8 Å (E) and z = 12 Å (F), the x-z plane at y = 0 Å (G) and the y-z plane at x = 0 Å (H).

bioRxiv preprint doi: https://doi.org/10.1101/2021.06.22.449380; this version posted June 23, 2021. The copyright holder for this preprint (which was not certified by peer review) is the author/funder, who has granted bioRxiv a license to display the preprint in perpetuity. It is made available under aCC-BY-NC-ND 4.0 International license.

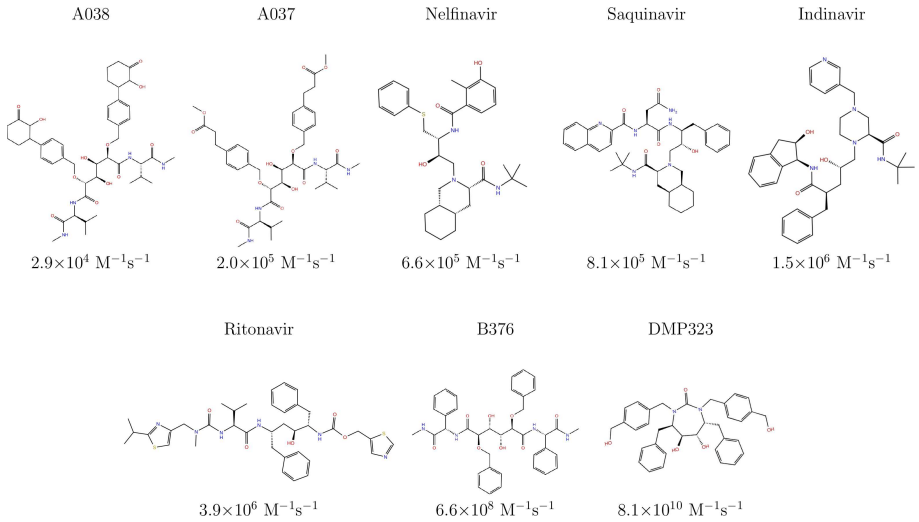

Fig 7. Chemical structures of the set of peptidomimetic ligands for which association rate constants were computed and which have a wide range of experimentally determined association rate constants, k_{on}^{exp} $\sim 10^4$ - 10^{10} $\mathrm{M^{-1}s^{-1}}$.

Table 1. Comparison of experimental association rate constants (k_{on}^{exp}) with computed ungated constants for individual (k_m^{ug}) and multiple-combined (k^{ug}) accessible states and corresponding gated rate constants (k^g), computed with a gating factor of $\gamma = 0.75$. All rate constants are given in units of $\mu\mathrm{M^{-1}s^{-1}}$.

Ligand	k_{C2}^{ug}	k_{C4}^{ug}	k_{C5}^{ug}	k^{ug}	k^g	k_{on}^{exp}
A038	417.00 ± 5.24	103.72 ± 1.50	330.67 ± 5.70	292.48 ± 4.27	219.36 ± 3.20	0.03 ± 0.00
A037	349.53 ± 2.81	89.69 ± 2.76	262.07 ± 5.66	240.71 ± 3.79	180.53 ± 2.84	0.20 ± 0.04
Nelfinavir	156.96 ± 3.70	84.54 ± 2.58	61.77 ± 0.80	101.89 ± 2.35	76.42 ± 1.76	0.66 ± 0.30
Saquinavir	103.56 ± 3.02	48.59 ± 3.21	32.32 ± 2.11	62.11 ± 2.76	46.58 ± 2.07	0.82 ± 0.16
Indinavir	1052.30 ± 8.50	269.74 ± 4.65	866.02 ± 10.31	751.50 ± 7.97	563.63 ± 5.98	1.53 ± 0.24
Ritonavir	242.21 ± 4.06	39.90 ± 1.28	250.47 ± 5.67	184.16 ± 3.79	138.12 ± 2.84	3.92 ± 0.11
B376	631.82 ± 6.36	112.97 ± 2.71	672.54 ± 4.10	489.77 ± 4.47	367.33 ± 3.35	205.00 ± 187.00
DMP323	533.32 ± 2.98	157.72 ± 2.26	480.90 ± 5.78	401.87 ± 3.74	301.40 ± 2.81	25200.00 ± 9990.00

bioRxiv preprint doi: https://doi.org/10.1101/2021.06.22.449380; this version posted June 23, 2021. The copyright holder for this preprint (which was not certified by peer review) is the author/funder, who has granted bioRxiv a license to display the preprint in perpetuity. It is made available under aCC-BY-NC-ND 4.0 International license.

Discussion and Conclusions

We have developed an approach to characterize the effects of gating by a multi-conformation protein consisting of subsets of accessible and inaccessible states on ligand association rate constants. Our approach first involves the construction of a kinetic network model of the apo-protein from atomistic MD simulations from which we identify meaningful conformations, compute their relative populations and interchange kinetics, structurally characterizing them in terms of ligand accessibility. We integrate the calculated first-order rate constants for conformational transitions into a multi-state gating theory from which we derive a characteristic timescale for conformational transitions (τ_c) and a gating factor γ. This factor modulates the association rate constants of ungated ligand binding to the subset of accessible conformations (k^{ug}) - which we compute here for a set of ligands from Brownian dynamics simulations - when τ_c is significantly slower than the characteristic timescale for diffusional encounter (τ_d) and enables us to quantify the degree of conformational gating by the protein.

Applied to HIV-1 protease, the kinetic network model of the apo-protein has macrostates corresponding to canonical crystallographic conformations - namely the well-characterized closed (C3) and semi-open (C4) states, as well as open (C2) and wide-open (C5) states previously reported from atomistic and coarse-grained simulations. It also reveals a previously unreported (C1) state (Figure 4). This latter conformation is an asymmetric doublet macrostate (C1a and C1b) in which the β-hairpin moiety, termed 'flap', of one monomer, reaches into and across the active site, making contacts with the opposite monomer and vice versa. These contacts are a mixture of those unique to the conformation (especially the flap tip I50 with the distal D30′), some only otherwise exhibited by the semi-open conformation, and others only otherwise by the closed conformation (Figure 5). Structural characterization reveals that only this state exhibits significant overlap in the averaged atomic density when superimposed with a putative natural substrate bound in the closed conformation. The other characterized states fit within an existing putative model of conformational change across the catalytic cycle [119] - preferring a semi-open state in the apo protein, transitioning to an open/wide-open state during ligand encounter, then to the closed bound reactive state, and finally via an open state again for product release, back to the semi-open state. Our results suggest that C1 sterically partitions the active site, thus we term it 'parted' here. It may therefore assist in separating post-cleavage peptide fragments that are no longer covalently connected - and thus be favoured during product release, especially as it lies structurally on the pathway between closed and semi-open. CGMD simulations have suggested product release can occur even in the closed conformation [120]. The parted conformation is kinetically disjoint from all other states except the semi-open in our apo-protein model - future atomistic simulations may reveal whether transition to the parted conformation from closed becomes kinetically favourable during product release.

Our kinetic model suggests that, individually, all of the macrostate conformations are almost thermodynamically indistinguishable from each other. The stationary distribution favours the subset of accessible (semi-open, open and wide-open) states, but even combined they are only ∼1 kcal/mol more favourable than the sum of inaccessible states (parted and closed). Furthermore, there is comparatively rapid interchange between semi-open, open and wide-open states on the sub-μs timescale whilst being an order of magnitude slower from these states to either parted or closed conformations. Interestingly, this results in a slow gating regime for ligand binding ($\tau_c >> \tau_d$), but because the calculated gating factor is not much smaller than unity ($\gamma = 0.75$), this can still be interpreted as the protease almost always being accessible or open to binding. This view broadly agrees with our previous study [86] but here, we can quantify the estimated timescale of transition from semi-open to wide-open to be ∼500 ns, in good agreement with a previous kinetic model [87]. However, our model also suggests an equi-

bioRxiv preprint doi: https://doi.org/10.1101/2021.06.22.449380; this version posted June 23, 2021. The copyright holder for this preprint (which was not certified by peer review) is the author/funder, who has granted bioRxiv a license to display the preprint in perpetuity. It is made available under aCC-BY-NC-ND 4.0 International license.

stable population for the wide-open conformation compared to the other conformations, rather than a rarely accessed state. The role of the wide-open state is still ambiguous as ligand binding does not seem to require it. Indeed, we find binding of almost all ligands studied here is faster to the open than to the wide-open state (Table 1). The relative stability of the wide-open state may instead be compatible with alternate roles. It has been observed that the protease makes direct non-specific interactions with the viral RNA - dramatically enhancing catalytic activity [121]. Whilst the mechanism for this remains unclear, the wide-open state may further modulate RNA binding and thus indirectly regulate catalysis. The immature HIV-1 ribonucleoprotein forms a phase-separated condensate that allows influx of protease for its subsequent maturation [122]. The conformational flexibility of the protease, including its ability to form the wide-open state may aid its mobility in such a crowded environment.

The approach reported here enables us to dissect the potential contributions of gated conformational selection from induced fit during the process of ligand binding. Here, we studied an array of inhibitors of HIV-1 protease whose association rate constants measured by surface plasmon resonance vary in the range: k_{on}^{exp} $\sim 10^4$ - 10^{10} $\mathrm{M^{-1}s^{-1}}$. However, the calculated gated rate constants (k^g) all lie within a narrow range from $\sim$0.5-5.7 $\times$ 10^8 $\mathrm{M^{-1}s^{-1}}$. For the majority of the inhibitors, $k^g >> k_{on}^{exp}$ (Table 1), conformationally gated diffusional association is fast and the overall binding process is expected to be rate limited by the subsequent induced fit step. This mechanism is compatible with earlier findings from CGMD simulations on ligand binding [89]. Only one inhibitor (B376), a small peptidomimetic, exhibits a computed gated rate constant similar to the experimental rate constant. Thus, the second induced fit step is likely to be very fast and binding is rate-limited by the conformational gating of diffusion into the active site. Inhibitors with rate constants in this range are likely to belong to the same class. Finally, the inhibitor DMP323 exhibits $k^g << k_{on}^{exp}$ and is therefore not limited by either the first conformational gating or second induced fit steps. Its rate constant exceeds the Smoluchowski diffusion limit - therefore experiencing no hindrance from first encounter to final binding. This may be due to a first induced fit step which allows first encounters distal from the binding site to rapidly direct the ligand to the final bound state, possibly by lower-dimensional diffusion. Previous MD simulations of a similar rapid binder with a $k_{on}^{exp} \sim 10^9$ $\mathrm{M^{-1}s^{-1}}$ have suggested such an initial induced fit step from the semi-open conformation [90, 91]. Similarly, another rationale for the existence of states such as the parted and wide-open may be to facilitate this rapid binding mode.

Although, HIV-1 protease ligands exhibit complex combinations of conformational gating and induced fit, other proteins with gated binding sites may be largely modulated by the gating itself. In such cases, our approach may extend beyond classification of different binding pathways, in addition to revealing binding mechanisms, and allow the computation of association rate constants that correlate with the overall experimental rate constants for different inhibitors. Finally, because our method only requires computing the apo-protein kinetics once from atomistic simulations and then using the extracted conformations for simulating the binding of each ligand using computationally inexpensive independent Brownian dynamics simulations that can be run in parallel, it could be effectively scaled for such protein systems for high-throughput ligand ranking.

Supporting information

Figure S1. (A) Generalized Chapman-Kolmogorov test and (B) Distribution of microstate observation probabilities (χ) projected onto the λ-space.

Table S1. Top five most likely microstates that represent each macrostate.

bioRxiv preprint doi: https://doi.org/10.1101/2021.06.22.449380; this version posted June 23, 2021. The copyright holder for this preprint (which was not certified by peer review) is the author/funder, who has granted bioRxiv a license to display the preprint in perpetuity. It is made available under aCC-BY-NC-ND 4.0 International license.

Figure S2. Centroids of most probable microstate of each macrostate in the λ-space.

Table S2. Hydrogen bonds between flap and alternate monomers.

Figure S3. Cross sections of superimposed volumetric density of natural peptide and protein from a complex of HIV-1 protease.

Table S3. Sidechain-sidechain contacts between flap and alternate monomers.

Figure S4. Representative docked structures of peptidomimetic ligands to macrostates of HIV-1 protease.

Acknowledgments

The authors thank Dr. Gaurav Ganotra for assistance in parameterizing the ligands, Dr. Ricard Argelaguet and Dr. Stefan Richter for technical assistance, Prof. Gianni De Fabritiis for sharing previous simulation trajectories from the GPUGRID project and Dr. Toni Giorgino, Prof. Gilles Mirambeau, Prof. Andreas Meyerhans and Dr. Neil J. Bruce for discussions. This work was supported by the EU/EFPIA Innovative Medicines Initiative (IMI) Joint Undertaking, K4DD (grant no. 115366 to R.C.W.), the European Union Horizon 2020 Framework Programme (https://ec.europa.eu/programmes/horizon2020/en) for Research and Innovation under the Specific Grant Agreement no. 720270 (Human Brain Project SGA1, to R.C.W.), the Volkswagen Foundation "Experiment! Funding Initiative" (grant no. 93874 to S.K.S.), the amfAR Mathilde Krim Fellowship in Basic Biomedical Research (grant no. 108680 to S.K.S.) and the Klaus Tschira Foundation.

References

1. de Ruiter A, Oostenbrink C. Advances in the calculation of binding free energies. Current opinion in structural biology. 2020;61:207–212.

2. Swinney DC. The role of binding kinetics in therapeutically useful drug action. Current opinion in drug discovery & development. 2009;12(1):31–39.

3. Schuetz DA, de Witte WEA, Wong YC, Knasmueller B, Richter L, Kokh DB, et al. Kinetics for Drug Discovery: an industry-driven effort to target drug residence time. Drug Discovery Today. 2017;22(6):896–911.

4. Collins FC, Kimball GE. Diffusion-controlled reaction rates. Journal of colloid science. 1949;4(4):425–437.

5. Stroppolo M, Falconi M, Caccuri A, Desideri A. Superefficient enzymes. Cellular and Molecular Life Sciences CMLS. 2001;58(10):1451–1460.

6. Barzykin A, Seki K, Tachiya M. Kinetics of diffusion-assisted reactions in microheterogeneous systems. Advances in colloid and interface science. 2001;89:47–140.

7. Schlosshauer M, Baker D. A general expression for bimolecular association rates with orientational constraints. The Journal of Physical Chemistry B. 2002;106(46):12079–12083.

bioRxiv preprint doi: https://doi.org/10.1101/2021.06.22.449380; this version posted June 23, 2021. The copyright holder for this preprint (which was not certified by peer review) is the author/funder, who has granted bioRxiv a license to display the preprint in perpetuity. It is made available under aCC-BY-NC-ND 4.0 International license.

8. Northrup SH, Erickson HP. Kinetics of protein-protein association explained by Brownian dynamics computer simulation. Proceedings of the National Academy of Sciences. 1992;89(8):3338–3342.

9. Song Y, Zhang Y, Shen T, Bajaj CL, McCammon JA, Baker NA. Finite element solution of the steady-state Smoluchowski equation for rate constant calculations. Biophysical Journal. 2004;86(4):2017–2029.

10. Shaul Y, Schreiber G. Exploring the charge space of protein–protein association: a proteomic study. Proteins: Structure, Function, and Bioinformatics. 2005;60(3):341–352.

11. Wade RC, Gabdoulline RR, Lüdemann SK, Lounnas V. Electrostatic steering and ionic tethering in enzyme–ligand binding: Insights from simulations. Proceedings of the National Academy of Sciences. 1998;95(11):5942–5949.

12. Gabdoulline RR, Kummer U, Olsen LF, Wade RC. Concerted simulations reveal how peroxidase compound III formation results in cellular oscillations. Biophysical journal. 2003;85(3):1421–1428.

13. McCammon JA, Northrup SH. Gated binding of ligands to proteins. Nature. 1981;293(5830):316–317.

14. Szabo A, Shoup D, Northrup SH, McCammon JA. Stochastically gated diffusion-influenced reactions. The Journal of Chemical Physics. 1982;77(9):4484–4493.

15. Chang CE, Shen T, Trylska J, Tozzini V, McCammon JA. Gated binding of ligands to HIV-1 protease: Brownian dynamics simulations in a coarse-grained model. Biophysical journal. 2006;90(11):3880–3885.

16. Boehr DD, Nussinov R, Wright PE. The role of dynamic conformational ensembles in biomolecular recognition. Nature chemical biology. 2009;5(11):789–796.

17. Silva DA, Bowman GR, Sosa-Peinado A, Huang X. A role for both conformational selection and induced fit in ligand binding by the LAO protein. PLoS Comput Biol. 2011;7(5):e1002054.

18. Changeux JP, Edelstein S. Conformational selection or induced fit? 50 years of debate resolved. F1000 biology reports. 2011;3.

19. Zhou HX. Theory of the diffusion-influenced substrate binding rate to a buried and gated active site. The Journal of chemical physics. 1998;108(19):8146–8154.

20. Zhou HX, Wlodek ST, McCammon JA. Conformation gating as a mechanism for enzyme specificity. Proceedings of the National Academy of Sciences. 1998;95(16):9280–9283.

21. Zhou HX, McCammon JA. The gates of ion channels and enzymes. Trends in biochemical sciences. 2010;35(3):179–185.

22. McCammon JA. Gated diffusion-controlled reactions. BMC biophysics. 2011;4(1):1–5.

23. Northrup SH, Allison SA, McCammon JA. Brownian dynamics simulation of diffusion-influenced bimolecular reactions. The Journal of Chemical Physics. 1984;80(4):1517–1524.

24. Gabdoulline RR, Wade RC. Simulation of the diffusional association of barnase and barstar. Biophysical journal. 1997;72(5):1917–1929.

bioRxiv preprint doi: https://doi.org/10.1101/2021.06.22.449380; this version posted June 23, 2021. The copyright holder for this preprint (which was not certified by peer review) is the author/funder, who has granted bioRxiv a license to display the preprint in perpetuity. It is made available under aCC-BY-NC-ND 4.0 International license.

25. Gabdoulline RR, Wade RC. Protein-protein association: investigation of factors influencing association rates by Brownian dynamics simulations. Journal of molecular biology. 2001;306(5):1139–1155.

26. Luty BA, El Amrani S, McCammon JA. Simulation of the bimolecular reaction between superoxide and superoxide dismutase: synthesis of the encounter and reaction steps. Journal of the American Chemical Society. 1993;115(25):11874–11877.

27. Sung JC, Wynsberghe AWV, Amaro RE, Li WW, McCammon JA. Role of secondary sialic acid binding sites in influenza N1 neuraminidase. Journal of the American Chemical Society. 2010;132(9):2883–2885.

28. Zeller F, Luitz MP, Bomblies R, Zacharias M. Multiscale simulation of receptor–drug association kinetics: Application to neuraminidase inhibitors. Journal of chemical theory and computation. 2017;13(10):5097–5105.

29. Votapka LW, Jagger BR, Heyneman AL, Amaro RE. SEEKR: simulation enabled estimation of kinetic rates, a computational tool to estimate molecular kinetics and its application to trypsin–benzamidine binding. The Journal of Physical Chemistry B. 2017;121(15):3597–3606.

30. Jagger BR, Lee CT, Amaro RE. Quantitative ranking of ligand binding kinetics with a multiscale milestoning simulation approach. The journal of physical chemistry letters. 2018;9(17):4941–4948.

31. Jagger BR, Ojha AA, Amaro RE. Predicting Ligand Binding Kinetics Using a Markovian Milestoning with Voronoi Tessellations Multiscale Approach. Journal of Chemical Theory and Computation. 2020;16(8):5348–5357.

32. Bruce NJ, Ganotra GK, Kokh DB, Sadiq SK, Wade RC. New approaches for computing ligand–receptor binding kinetics. Current opinion in structural biology. 2018;49:1–10.

33. Nunes-Alves A, Kokh DB, Wade RC. Recent progress in molecular simulation methods for drug binding kinetics. Current Opinion in Structural Biology. 2020;64:126–133.

34. De Vivo M, Masetti M, Bottegoni G, Cavalli A. Role of molecular dynamics and related methods in drug discovery. Journal of medicinal chemistry. 2016;59(9):4035–4061.

35. Buch I, Giorgino T, De Fabritiis G. Complete reconstruction of an enzyme-inhibitor binding process by molecular dynamics simulations. Proceedings of the National Academy of Sciences. 2011;108(25):10184–10189.

36. Gu S, Silva DA, Meng L, Yue A, Huang X. Quantitatively characterizing the ligand binding mechanisms of choline binding protein using Markov state model analysis. PLoS Comput Biol. 2014;10(8):e1003767.

37. Plattner N, Noé F. Protein conformational plasticity and complex ligand-binding kinetics explored by atomistic simulations and Markov models. Nature communications. 2015;6(1):1–10.

38. Paul F, Wehmeyer C, Abualrous ET, Wu H, Crabtree MD, Schöneberg J, et al. Protein-peptide association kinetics beyond the seconds timescale from atomistic simulations. Nature communications. 2017;8(1):1–10.

bioRxiv preprint doi: https://doi.org/10.1101/2021.06.22.449380; this version posted June 23, 2021. The copyright holder for this preprint (which was not certified by peer review) is the author/funder, who has granted bioRxiv a license to display the preprint in perpetuity. It is made available under aCC-BY-NC-ND 4.0 International license.

39. Plattner N, Doerr S, De Fabritiis G, Noé F. Complete protein–protein association kinetics in atomic detail revealed by molecular dynamics simulations and Markov modelling. Nature chemistry. 2017;9(10):1005.

40. Noé F, Schütte C, Vanden-Eijnden E, Reich L, Weikl TR. Constructing the equilibrium ensemble of folding pathways from short off-equilibrium simulations. Proceedings of the National Academy of Sciences. 2009;106(45):19011–19016.

41. Voelz VA, Bowman GR, Beauchamp K, Pande VS. Molecular simulation of ab initio protein folding for a millisecond folder NTL9 (1- 39). Journal of the American Chemical Society. 2010;132(5):1526–1528.

42. Bowman GR, Pande VS. Protein folded states are kinetic hubs. Proceedings of the National Academy of Sciences. 2010;107(24):10890–10895.

43. Sborgi L, Verma A, Piana S, Lindorff-Larsen K, Cerminara M, Santiveri CM, et al. Interaction networks in protein folding via atomic-resolution experiments and long-time-scale molecular dynamics simulations. Journal of the American Chemical Society. 2015;137(20):6506–6516.

44. Sadiq SK, Noé F, De Fabritiis G. Kinetic characterization of the critical step in HIV-1 protease maturation. Proceedings of the National Academy of Sciences. 2012;109(50):20449–20454.

45. Xia J, Deng Nj, Levy RM. NMR relaxation in proteins with fast internal motions and slow conformational exchange: model-free framework and Markov state simulations. The Journal of Physical Chemistry B. 2013;117(22):6625–6634.

46. Shukla D, Meng Y, Roux B, Pande VS. Activation pathway of Src kinase reveals intermediate states as targets for drug design. Nature communications. 2014;5(1):1–11.

47. Banerjee R, Yan H, Cukier RI. Conformational transition in signal transduction: metastable states and transition pathways in the activation of a signaling protein. The Journal of Physical Chemistry B. 2015;119(22):6591–6602.

48. Perkett MR, Hagan MF. Using Markov state models to study self-assembly. The Journal of chemical physics. 2014;140(21):214101.

49. Chodera JD, Noé F. Markov state models of biomolecular conformational dynamics. Current opinion in structural biology. 2014;25:135–144.

50. Noé F, Wu H, Prinz JH, Plattner N. Projected and hidden Markov models for calculating kinetics and metastable states of complex molecules. The Journal of chemical physics. 2013;139(18):184114.

51. Prinz JH, Wu H, Sarich M, Keller B, Senne M, Held M, et al. Markov models of molecular kinetics: Generation and validation. The Journal of chemical physics. 2011;134(17):174105.

52. Husic BE, Pande VS. Markov state models: From an art to a science. Journal of the American Chemical Society. 2018;140(7):2386–2396.

53. Noé F, Nuske F. A variational approach to modeling slow processes in stochastic dynamical systems. Multiscale Modeling & Simulation. 2013;11(2):635–655.

54. Naritomi Y, Fuchigami S. Slow dynamics in protein fluctuations revealed by time-structure based independent component analysis: the case of domain motions. The Journal of chemical physics. 2011;134(6):065101.

bioRxiv preprint doi: https://doi.org/10.1101/2021.06.22.449380; this version posted June 23, 2021. The copyright holder for this preprint (which was not certified by peer review) is the author/funder, who has granted bioRxiv a license to display the preprint in perpetuity. It is made available under aCC-BY-NC-ND 4.0 International license.

55. Schwantes CR, Pande VS. Improvements in Markov state model construction reveal many non-native interactions in the folding of NTL9. Journal of chemical theory and computation. 2013;9(4):2000–2009.

56. Pérez-Hernández G, Paul F, Giorgino T, De Fabritiis G, Noé F. Identification of slow molecular order parameters for Markov model construction. The Journal of chemical physics. 2013;139(1):015102.

57. Bowman GR, Ensign DL, Pande VS. Enhanced modeling via network theory: Adaptive sampling of Markov state models. Journal of chemical theory and computation. 2010;6(3):787–794.

58. Doerr S, De Fabritiis G. On-the-fly learning and sampling of ligand binding by high-throughput molecular simulations. Journal of chemical theory and computation. 2014;10(5):2064–2069.

59. Hruska E, Abella JR, Nüske F, Kavraki LE, Clementi C. Quantitative comparison of adaptive sampling methods for protein dynamics. The Journal of chemical physics. 2018;149(24):244119.

60. Mardt A, Pasquali L, Wu H, Noé F. VAMPnets for deep learning of molecular kinetics. Nature communications. 2018;9(1):1–11.

61. Cavalli A, Spitaleri A, Saladino G, Gervasio FL. Investigating drug–target association and dissociation mechanisms using metadynamics-based algorithms. Accounts of chemical research. 2015;48(2):277–285.

62. Tiwary P, Limongelli V, Salvalaglio M, Parrinello M. Kinetics of protein–ligand unbinding: Predicting pathways, rates, and rate-limiting steps. Proceedings of the National Academy of Sciences. 2015;112(5):E386–E391.

63. Pietrucci F, Marinelli F, Carloni P, Laio A. Substrate binding mechanism of HIV-1 protease from explicit-solvent atomistic simulations. Journal of the American Chemical Society. 2009;131(33):11811–11818.

64. Wang J, Miao Y. Peptide Gaussian accelerated molecular dynamics (PepGaMD): Enhanced sampling and free energy and kinetics calculations of peptide binding. The Journal of Chemical Physics. 2020;153(15):154109.

65. Dickson A, Lotz SD. Multiple ligand unbinding pathways and ligand-induced destabilization revealed by WExplore. Biophysical journal. 2017;112(4):620–629.

66. Mollica L, Decherchi S, Zia SR, Gaspari R, Cavalli A, Rocchia W. Kinetics of protein-ligand unbinding via smoothed potential molecular dynamics simulations. Scientific reports. 2015;5(1):1–12.

67. Teo I, Mayne CG, Schulten K, Lelièvre T. Adaptive multilevel splitting method for molecular dynamics calculation of benzamidine-trypsin dissociation time. Journal of chemical theory and computation. 2016;12(6):2983–2989.

68. Miao Y. Acceleration of biomolecular kinetics in Gaussian accelerated molecular dynamics. The Journal of chemical physics. 2018;149(7):072308.

69. Wlodawer A, Miller M, Jaskólski M, Sathyanarayana BK, Baldwin E, Weber IT, et al. Conserved folding in retroviral proteases: crystal structure of a synthetic HIV-1 protease. Science. 1989;245:616–621.

bioRxiv preprint doi: https://doi.org/10.1101/2021.06.22.449380; this version posted June 23, 2021. The copyright holder for this preprint (which was not certified by peer review) is the author/funder, who has granted bioRxiv a license to display the preprint in perpetuity. It is made available under aCC-BY-NC-ND 4.0 International license.

70. Prabu-Jeyabalan M, Nalivaika E, Schiffer CA. How does a symmetric dimer recognize an asymmetric substrate? A substrate complex of HIV-1 protease. J Mol Biol. 2000;301:1207–1220.

71. Prabu-Jeyabalan M, Nalivaika E, Schiffer CA. Substrate shape determines specificity of recognition for HIV-1 protease: Analysis of crystal structures of six substrate complexes. Structure. 2002;10:369–381.

72. Pettit SC, Sheng N, Tritch R, Erickson-Viitanen S, Swanstrom R. The regulation of sequential processing of HIV-1 gag by the viral protease. Advances in Experimental Medicine and Biology. 1998;436:15–25.

73. Pettit SC, Henderson GJ, Schiffer CA, Swanstrom R. Replacement of the P1 amino acid of human immunodeficiency virus type 1 gag processing sites can inhibit or enhance the rate of cleavage by the viral protease. J Virol. 2002;76(20):10226–10233.

74. Pettit SC, Clemente JC, Jeung JA, Dunn BM, Kaplan AH. Ordered processing of the human immunodeficiency virus type 1 gagpol precursor is influenced by the context of the embedded viral protease. Journal of Virology. 2005;79(16):10601–10607.

75. Palese LL. Conformations of the HIV-1 protease: a crystal structure data set analysis. Biochimica et Biophysica Acta (BBA)-Proteins and Proteomics. 2017;1865(11):1416–1422.

76. Hassan S, Srikakulam SK, Chandramohan Y, Thangam M, Muthukumar S, Gayathri Devi P, et al. Exploring the conformational landscapes of HIV protease structural ensembles using principal component analysis. Proteins: Structure, Function, and Bioinformatics. 2018;86(9):990–1000.

77. Spinelli S, Liu Q, Alzari P, Hirel P, Poljak R. The three-dimensional structure of the aspartyl protease from the HIV-1 isolate BRU. Biochimie. 1991;73(11):1391–1396.

78. Martin P, Vickrey JF, Proteasa G, Jimenez YL, Wawrzak Z, Winters MA, et al. "Wide-open" 1.3 A structure of a multidrug-resistant HIV-1 protease as a drug target. Structure. 2005;13(12):1887–1895. doi:10.1016/j.str.2005.11.005.

79. Torbeev VY, Raghuraman H, Hamelberg D, Tonelli M, Westler WM, Perozo E, et al. Protein conformational dynamics in the mechanism of HIV-1 protease catalysis. Proceedings of the National Academy of Sciences. 2011;108(52):20982–20987.

80. Ishima R, Freedberg DI, Wang YX, Louis JM, Torchia DA. Flap opening and dimer-interface flexibility in the free and inhibitor-bound HIV protease, and their implications for function. Structure. 1999;7:1047–1055.

81. Freedberg DI, Ishima R, Jacob J, Wang YX, Kustanovich I, Louis JM, et al. Rapid structural fluctuations of the free HIV protease flaps in solution: Relationship to crystal structures and comparison with predictions of dynamics calculations. Protein Sci. 2002;11:221–232.

82. Roche J, Louis JM, Bax A. Conformation of inhibitor-free HIV-1 protease derived from nmr spectroscopy in a weakly oriented solution. ChemBioChem. 2015;16(2):214–218.

bioRxiv preprint doi: https://doi.org/10.1101/2021.06.22.449380; this version posted June 23, 2021. The copyright holder for this preprint (which was not certified by peer review) is the author/funder, who has granted bioRxiv a license to display the preprint in perpetuity. It is made available under aCC-BY-NC-ND 4.0 International license.

83. Sadiq SK, Wan S, Coveney PV. Insights into a mutation-assisted lateral drug escape mechanism from the HIV-1 protease active site. Biochemistry. 2007;46:14865–14877.

84. Chang CEA, Trylska J, Tozzini V, Andrew McCammon J. Binding pathways of ligands to HIV-1 protease: coarse-grained and atomistic simulations. Chemical biology & drug design. 2007;69(1):5–13.

85. Hornak V, Okur A, Rizzo RC, Simmerling C. HIV-1 protease flaps spontaneously close to the correct structure in simulations following manual placement of an inhibitor into the open state. J Am Chem Soc. 2006;128(9):2812–2813. doi:10.1021/ja058211x.

86. Sadiq SK, De Fabritiis G. Explicit solvent dynamics and energetics of HIV-1 protease flap opening and closing. Proteins. 2010;78(14):2873–2885. doi:10.1002/prot.22806.

87. Deng Nj, Zheng W, Gallicchio E, Levy RM. Insights into the dynamics of HIV-1 protease: a kinetic network model constructed from atomistic simulations. Journal of the American Chemical Society. 2011;133(24):9387–9394.

88. Markgren PO, Schaal W, Hämäläinen M, Karlén A, Hallberg A, Samuelsson B, et al. Relationships between structure and interaction kinetics for HIV-1 protease inhibitors. Journal of medicinal chemistry. 2002;45(25):5430–5439.

89. Kang M, Roberts C, Cheng Y, Chang CeA. Gating and intermolecular interactions in ligand-protein association: coarse-grained modeling of HIV-1 protease. Journal of chemical theory and computation. 2011;7(10):3438–3446.

90. Huang YmM, Raymundo MAV, Chen W, Chang CeA. Mechanism of the association pathways for a pair of fast and slow binding ligands of HIV-1 protease. Biochemistry. 2017;56(9):1311–1323.

91. Miao Y, Huang YmM, Walker RC, McCammon JA, Chang CeA. Ligand binding pathways and conformational transitions of the HIV protease. Biochemistry. 2018;57(9):1533–1541.

92. Scherer MK, Trendelkamp-Schroer B, Paul F, Pérez-Hernández G, Hoffmann M, Plattner N, et al. PyEMMA 2: A software package for estimation, validation, and analysis of Markov models. Journal of chemical theory and computation. 2015;11(11):5525–5542.

93. Berman HM, Westbrook J, Feng Z, Gilliland G, Bhat TN, Weissig H, et al. The protein data bank. Nucleic Acids Res. 2000;28:235–242.

94. Duan Y, Wu C, Chowdhury S, Lee MC, Xiong G, Zhang W, et al. A point-charge force field for molecular mechanics simulations of proteins based on condensed-phase quantum mechanical calculations. J Comput Chem. 2003;24:1999–2012.

95. Hyland LJ, Tomaszek TA Jr, Meek TD. Human immunodeficiency virus-1 protease. 2. Use of pH rate studies and solvent kinetic isotope effects to elucidate details of chemical mechanism. Biochemistry. 1991;30:8454–8463.

96. Wang YX, Freedberg DI, Yamazaki T, Wingfield PT, Stahl SJ, Kaufman JD, et al. Solution NMR evidence that the HIV-1 protease catalytic aspartyl groups have different ionization states in the complex formed with the Asymmetric drug KNI-272. Biochemistry. 1996;35(31):9945–9950.

bioRxiv preprint doi: https://doi.org/10.1101/2021.06.22.449380; this version posted June 23, 2021. The copyright holder for this preprint (which was not certified by peer review) is the author/funder, who has granted bioRxiv a license to display the preprint in perpetuity. It is made available under aCC-BY-NC-ND 4.0 International license.

97. Kovalskyy D, Dubyna V, Mark AE, Korenelyuk A. A molecular dynamics study of the structural stability of HIV-1 protease under physiological conditions: The role of Na+ ions in stabilizing the active site. Proteins: Struct Funct Bioinf. 2005;58:450–458.

98. Wittayanarakul K, Hannongbua S, Feig M. Accurate prediction of protonation state as a prerequisite for reliable MM-PB(GB)SA binding free energy calculations of HIV-1 protease inhibitors. J Comput Chem. 2008;29(5):673–685. doi:10.1002/jcc.20821.

99. Humphrey W, Dalke A, Schulten K. VMD - Visual molecular dynamics. J Mol Graphics. 1996;14:33–38.

100. Pearlman DA, Case DA, Caldwell JW, Ross WS, Cheatham TE III, DeBolt S, et al. AMBER, a package of computer programs for applying molecular mechanics, normal mode analysis, molecular dynamics and free energy calculations to simulate the structural and energetic properties of molecules. Comput Phys Comm. 1995;91:1–41.

101. Jorgensen WL, Chandrasekhar J, Madura JD, Impey RW, Klein ML. Comparison of simple potential functions for simulating liquid water. J Chem Phys. 1983;79:926–935.

102. Harvey MJ, Giupponi G, Fabritiis GD. ACEMD: Accelerating Biomolecular Dynamics in the Microsecond Time Scale. J Chem Theor Comput. 2009;5(6):1632–1639. doi:10.1021/ct9000685.

103. Meagher KL, Carlson HA. Solvation Influences Flap Collapse in HIV-1 Protease. Proteins: Struct Funct Bioinf. 2005;58:119–125.

104. Harvey M, De Fabritiis G. An implementation of the smooth particle mesh ewald method on gpu hardware. Journal of Chemical Theory and Computation. 2009;5(9):2371–2377.

105. Essmann U, Perera L, Berkowitz ML, Darden T. A smooth particle mesh Ewald method. J Chem Phys. 1995;103:8577–9593.

106. Ryckaert JP, Ciccotti G, Berendsen HJC. Numerical integration of the Cartesian equations of motion of a system with constraints: Molecular dynamics of n-alkanes. J Comput Phys. 1977;23:327–341.

107. Feenstra KA, Hess B, Berendsen HJC. Improving efficiency of large time-scale molecular dynamics simulations of hydrogen-rich systems. J Comput Chem. 1999;20(8):786–798.

108. Sadiq SK, Coveney PV. Computing the role of near attack conformations in an enzyme-catalyzed nucleophilic bimolecular reaction. Journal of chemical theory and computation. 2015;11(1):316–324.

109. Sadiq SK. Fine-Tuning of Sequence Specificity by Near Attack Conformations in Enzyme-Catalyzed Peptide Hydrolysis. Catalysts. 2020;10(6):684.

110. Michaud-Agrawal N, Denning EJ, Woolf TB, Beckstein O. MDAnalysis: a toolkit for the analysis of molecular dynamics simulations. Journal of computational chemistry. 2011;32(10):2319–2327.

bioRxiv preprint doi: https://doi.org/10.1101/2021.06.22.449380; this version posted June 23, 2021. The copyright holder for this preprint (which was not certified by peer review) is the author/funder, who has granted bioRxiv a license to display the preprint in perpetuity. It is made available under aCC-BY-NC-ND 4.0 International license.

111. Maier JA, Martinez C, Kasavajhala K, Wickstrom L, Hauser KE, Simmerling C. ff14SB: improving the accuracy of protein side chain and backbone parameters from ff99SB. Journal of chemical theory and computation. 2015;11(8):3696–3713.

112. Ganotra GK, Wade RC. Prediction of drug–target binding kinetics by comparative binding energy analysis. ACS medicinal chemistry letters. 2018;9(11):1134–1139.

113. Case D, Ben-Shalom I, Brozell S, Cerutti D, Cheatham III T, Cruzeiro V, et al. AMBER 2018. University of California, San Francisco. 2018;.

114. Baker NA, Sept D, Joseph S, Holst MJ, McCammon JA. Electrostatics of nanosystems: application to microtubules and the ribosome. Proceedings of the National Academy of Sciences. 2001;98(18):10037–10041.

115. Martinez M, Bruce NJ, Romanowska J, Kokh DB, Ozboyaci M, Yu X, et al. SDA 7: A modular and parallel implementation of the simulation of diffusional association software. Journal of computational chemistry. 2015;36(21):1631–1645.

116. Gabdoulline RR, Wade RC. Effective charges for macromolecules in solvent. The Journal of Physical Chemistry. 1996;100(9):3868–3878.

117. Ganotra GK. Computational studies of drug-binding kinetics. Heidelberg University; 2020.

118. de la Torre JG, Huertas ML, Carrasco B. Calculation of hydrodynamic properties of globular proteins from their atomic-level structure. Biophysical journal. 2000;78(2):719–730.

119. Karthik S, Senapati S. Dynamic flaps in HIV-1 protease adopt unique ordering at different stages in the catalytic cycle. Proteins: Structure, Function, and Bioinformatics. 2011;79(6):1830–1840.

120. Trylska J, Tozzini V, Chang CeA, McCammon JA. HIV-1 protease substrate binding and product release pathways explored with coarse-grained molecular dynamics. Biophys J. 2007;92(12):4179–4187. doi:10.1529/biophysj.106.100560.

121. Potempa M, Nalivaika E, Ragland D, Lee SK, Schiffer CA, Swanstrom R. A direct interaction with RNA dramatically enhances the catalytic activity of the HIV-1 protease in vitro. Journal of molecular biology. 2015;427(14):2360–2378.

122. Lyonnais S, Sadiq SK, Lorca-Oró C, Dufau L, Nieto-Marquez S, Escriba T, et al. The HIV-1 ribonucleoprotein dynamically regulates its condensate behavior and drives acceleration of protease activity through membrane-less granular phase-separation. bioRxiv. 2019; p. 528638.